ORIGINAL ARTICLE

The role of the strengthening phases on the HAZ liquation cracking in a cast Ni-based superalloy used in industrial gas turbines

Łukasz Rakoczy[1] · Małgorzata Grudzień-Rakoczy[2] · Bogdan Rutkowski[1] · Rafał Cygan[3] · Fabian Hanning[4] · Grzegorz Cios[5] · Stefan Habisch[6] · Joel Andersson[4] · Peter Mayr[6] · Anna Zielińska-Lipiec[1]

Abstract

This work presents the influence of microstructural constituents on liquation crack formation in the cast Ni-based superalloy, René 108. The investigation was divided into three parts: characterisation of the material's microstructure in pre-weld condition, hot ductility studies and analysis of liquation cracking induced by the gas tungsten arc welding process. Using advanced electron microscopy techniques it is shown that the base material in pre-weld condition is characterised by a complex microstructure. The phases identified in René 108 include γ matrix, γ' precipitates, MC and $M_{23}C_6$ carbides, and M_5B_3 borides. Based on Gleeble testing, it was found that René 108 is characterised by high strength at elevated temperatures with a maximum of 1107 MPa at 975 °C. As a result of constitutional liquation, the superalloy's strength and ductility were significantly reduced. The nil strength temperature was equal to 1292 °C, while the nil ductility temperature was 1225 °C. The low ductility recovery rate (32.1), ratio of ductility recovery (36.2) and hot cracking factor ($R_f = 0.05$) values confirmed the low weldability of Renè 108. In the heat-affected zone (HAZ) induced by welding, constitutional liquation of mainly γ' precipitates, with a contribution of $M_{23}C_6$ carbides and M_5B_3 borides, was observed. The thin non-equilibrium liquid film, which formed along high-angle grain boundaries, led to crack initiation and their further propagation during cooling. The eutectic γ–γ' re-solidification products are visible on the crack edges.

Keywords Constitutional liquation · Liquation cracking · Superalloy · René 108 · STEM

1 Introduction

The unique combination of high strength and resistance to oxidation and hot corrosion make Ni-based superalloys one of the most important materials in constructing industrial gas turbine components, like blades, buckets and vanes [1, 2]. The main production process of Ni-base superalloy components is vacuum investment casting in ceramic shell moulds. The advantage of this process is the ability to reproduce geometrically complex elements made of difficult-to-shape materials in terms of machining and welding. Apart from strict dimensional tolerances, one of the leading quality criteria is the absence of casting defects on the external working surfaces [3, 4]. In most cases, repairing a defective component would be more economically advantageous than a direct replacement. The use of welding or cladding is desirable for increasing manufacturing process efficiency and repairing serviced components to extend their lifetime [5]. Unfortunately, this is very challenging due to the high susceptibility of Ni-based superalloys to liquation cracking

✉ Łukasz Rakoczy
  lrakoczy@agh.edu.pl

[1] Faculty of Metals Engineering and Industrial Computer Science, AGH University of Science and Technology, Mickiewicza 30, 30-059 Kraków, Poland

[2] Łukasiewicz Research Network-Kraków Institute of Technology, Zakopiańska 73, 30-418 Kraków, Poland

[3] Investment Casting Division, Consolidated Precision Products Corporation, Hetmańska 120, 35-078 Rzeszów, Poland

[4] Department of Engineering Science, University West, Gustava Melins Gata 2, 46132 Trollhättan, Sweden

[5] Academic Centre for Materials and Nanotechnology, AGH University of Science and Technology, Mickiewicza 30, 30-059 Kraków, Poland

[6] Chair of Materials Engineering of Additive Manufacturing, Technical University of Munich, Boltzmannstr. 15, 85748 Garching/Munich, Germany

during welding. Solidification cracks in the fusion zone are also observed, however, they are not as problematic as cracks in the heat-affected zone (HAZ). Cracking in the fusion zone can be eliminated by the appropriate filler metal, however, the chemical composition and microstructure of the base material, in most cases, cannot be arbitrarily changed. Liquation cracks in HAZs are significantly more challenging, as numerous strengthening phases, characterised by a complex chemical composition that decrease weldability, contribute to their occurrence. Nevertheless, these phases are necessary to achieve stability and heat resistance during long-term service. Ni-based superalloys containing substantial amounts of Al and Ti (more than 6 wt%) are generally considered very difficult to weld due to their high susceptibility to cracking [6–9]. This criterion does not consider other microstructural constituents like carbides and borides. Therefore, superalloys with theoretically good weldability unexpectedly crack during welding or repairing. A characteristic feature of Ni-based superalloys is a complex chemical composition resulting from more than 10 alloying elements with significantly different physico-chemical properties. This leads to the formation of various phases, usually with complex morphologies and a high tendency to segregation [10]. Therefore, the weldability of each superalloy should be considered individually. The mechanism, by which liquid forms, has been attributed to the constitutional liquation of strengthening precipitates. A mechanism of constitutional liquation, first proposed by Pepe and Savage, has been broadly presented in several works [11]. Constitutional liquation is generally understood to be a type of liquid formation that occurs at the interface of a precipitate/matrix, resulting in a thin film of liquid with non-equilibrium composition enriched in alloying elements at a temperature equal to or higher than the eutectic temperature. The theory assumes that thermodynamic equilibrium is maintained at the precipitate/matrix interface during dissolution and at the precipitate/liquid and liquid/matrix interface during fusing. This means that these processes are controlled by diffusion. Radhakrishnan [12] suggested that when solid-state dissolution is fully controlled by the mobility of the interface (coherent precipitations), precipitate/matrix interface enrichment with an alloying element required to initiate concentration melting is much lower. The equilibrium concentration determined by the solvus curve is only achievable when this boundary has unlimited mobility. Deviation from equilibrium decreases at higher temperatures as the mobility of the interface increases with temperature. Local deviation from thermodynamic equilibrium at the shifting interphase boundaries has been observed in many two-component systems [13, 14].

This work aims to reveal the contribution of microstructural constituents to the susceptibility to liquation crack formation in the equiaxed Ni-based superalloy, René 108. This grade is characterised by a very complex chemical composition compared to other popular Ni-based superalloys. To understand the behaviour of the exceptionally complex Ni-based superalloys during welding, it is necessary to fully investigate their microstructure in pre-weld condition. The detection and characterisation of even nanoprecipitates are essential in liquation cracking analysis. Without knowledge on the phase composition in pre-weld condition, it is problematic to predict non-equilibrium phase transformations. Experiments were carried out to clarify the contribution of each strengthening precipitate in the constitutional liquation of the Ni-based superalloy René 108. The obtained results will contribute to filling the existing knowledge gap on the weldability of the René 108 and ensure a better understanding of microstructural changes in the heat-affected zone.

2 Experimental procedure

The René 108 superalloy was used in this study and its chemical composition is presented in Table 1.

The material was manufactured through lost-wax casting and subjected to full heat treatment under vacuum (solution: 1200—2 h; ageing: 900—8 h). The cross-sectioned samples of René 108 in pre-weld condition were subjected to standard metallographic preparation. They were mounted in resin, ground on SiC papers (#120, #240, #500, #800, #1200, #2000, #3000, #4000) and polished on diamond suspensions (3 μm pre-polishing, 1 μm final) and silica oxide (0.06 μm). The specimens were electrolytically etched in a 10% aqueous solution of oxalic acid (Oxalic). Microstructure observations were carried out via light microscopy (LM, LEICA DM 4000 M) and scanning electron microscopy (SEM, Phenom XL). An accelerating voltage of 20 kV was used together with a back-scattered electron detector (BSE). The size of secondary γ' precipitates in dendritic regions was represented as the precipitates' square side (square root of precipitates' area). The measurements were carried out in 10 locations based on images captured at ×25,000 magnification (area of 114.49 μm^2). The SEM-BSE images were

Table 1 Chemical composition of the René 108 Ni-based superalloy, wt %

Element	Cr	W	Co	Al	Ta	Hf	Ti	Mo	C	B	Zr	V	Fe	Si	Ni	Others
Concentration	11.40	8.85	8.19	6.35	3.55	1.52	0.75	0.45	0.08	0.015	0.014	0.04	0.07	0.04	Bal	P-0.006
Standard deviation	0.08	0.04	0.04	0.08	0.09	0.06	0.008	0.006	0.001	0.0015	0.0004	0.002	0.0003	0.003		S-0.0002

binarized and subjected to a de-speckle filter, which removed noise without edge blurring. The area (A) and perimeter (P) of each γ' precipitate (assumed area range 0.02–4.0 μm^2) were selected. The superalloy's microstructure in pre-weld condition was additionally investigated by high-angle annular dark-field scanning transmission electron microscopy (HAADF-STEM). Ion polishing was applied to prepare the samples. First, the slices were ground to a thickness of about 50 um. Subsequently, discs with a 3 mm diameter were punched and dimpled with a Gatan Dimple Grinder on each side. The final step was thinning by an Ar$^+$ ion beam (PIPS of Gatan). The preparation of thin lamellae from grain boundaries (heat-affected zone) consisted of cutting out samples via focussed ion beam (FIB) using Ga$^+$ ions in a Thermo Fisher Scios 2 DualBeam FIB-SEM, equipped with a field emission gun and Ga$^+$ ion source. The lamellas were ion polished down to a thickness of 100 nm. Prior to observations, the thin foils were directly cleaned by a plasma cleaner to remove surface contaminations. Observations were carried out using a probe Cs-corrected Titan^3 G-2 60–300 with a ChemiSTEM system (Thermo Fisher Scientific) operating at 300 kV. Selected area electron diffractions (SAED) and images in the atomic-scale resolution after Fast Fourier Transformation (FFT) were analysed with the JEMS software.

The ThermoCalc software (version 2022a, Stockholm, Sweden), with the TCNI10 database, was used to analyse phase stability with increasing temperature under equilibrium conditions. Differential scanning calorimetry (DSC) tests were carried out using the SDT Q600 calorimeter by TA Instruments to determine the phase transformation temperatures in the superalloy during heating. The cube-shaped samples weighing 40 mg were placed in alumina crucibles and heated to 1500 °C at a rate of 10 °/min. The temperature was controlled with an S-type Pt/PtRh thermocouple. The Ar flow rate was 80 ml/min.

A Gleeble®3800 device was used for hot ductility tests. The aim was to investigate the susceptibility for hot cracking in the HAZ by liquation cracks and to quantify high-temperature ductility, measured as area reduction when simulating the welding process's thermal cycle of rapid heating and cooling (Fig. 1). The temperature was controlled via resistance heating combined with jaw-to-jaw heat conduction and compressed argon gas. During heating, materials usually experienced a drop in ductility, which characterises the onset of liquation in the material. The ductility decreases further as the temperature increases and reaches zero at the nil ductility temperature (NDT). As the temperature increases, the nil strength temperature (NST) is reached, where the superalloy does not possess any strength. The latter is used for defining the starting point of on-cooling tests. The NST was measured by subjecting cylindrical specimens with dimensions of
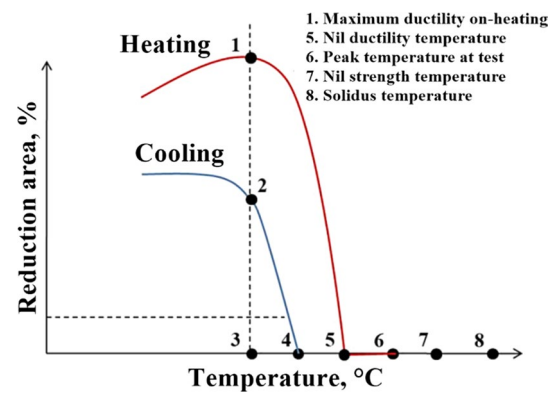

Fig. 1 The characteristic points in the hot ductility study [15]

90 mm × 6 mm to a constant 0.08 kN load, while being heated at a rate of 22.5 °C/s to 1150 °C and then at a rate of 3.33 °C/s until breaking. Hot ductility was measured on-heating and on cooling using threaded specimens with dimensions of 116.5 mm × 6 mm. The heating rate to the set temperature (below NST) was 111 °C/s, the holding time at peak temperature was 0.03 s, and the stroke rate was 55 mm/s. The on-heating tests included 11 temperatures in a range of 950–1250 °C. The on-cooling ductility was determined when each sample was first heated to the NST temperature minus 30 °C, followed by cooling to the desired testing temperature (from 1200–975 °C) at a rate of 50 °C/s. From the cooling tests, the ductility recovery temperature (DRT) is obtained, defined as the temperature, at which the reduction area has recovered to greater than 5%. Based on the collected data, the following was determined:(a) Brittle temperature range (BTR): difference between NST-40 °C and DTR,(b) Ductility recovery rate (DRR): the difference between the maximum reduction area obtained during heating and the corresponding value at this temperature during cooling (expressed in %),(c) The ratio of ductility recovery (RDR): the difference between the areas of 1-3-5 and 1-2-3 (expressed in %)(d) Hot crack resistance coefficient R$_f$ according to Eq. 1:

$$R_f = \frac{T_L - NST}{NST}, \quad T_L - \text{the liquidus temperature} \qquad (1)$$

To analyse the liquation cracking behaviour of the René 108 superalloys, specimens were subjected to bead-on-plate welding trials via gas tungsten arc welding (GTAW) with an Oerlikon device. Specimens with dimensions of 10 mm × 10 mm × 100 mm were cut off from the cast by wire electro-discharge machining (EDM) and then ground and cleaned in acetone to remove surface oxides. The following welding parameters were used: current 50 A, voltage 12 V, speed 180 mm/min. The bead-on-plate

specimens were sectioned transversely to the welding direction to produce samples for microstructural examination. Particular attention was paid to areas close to the liquation cracks, while focussing on precipitate identification, dissolution processes assessment and crack morphology characterisation. Additional crack edge observations under high magnification was carried out with a FEI VERSA 3D field emission SEM. Selected regions of the liquated areas were also subjected to crystallographic orientation analysis by back-scattered electron diffraction (EBSD) using a Hikari XP detector (EDAX). The used software was Team ver. 4.5 (EDAX), whereas OIM Analysis ver. 7.0 (EDAX) was used for generated figure analysis.

3 Results and discussion

3.1 Microstructure of René 108 in pre-weld condition

Figure 2 presents the change in the phase volume fraction as a function of temperature under equilibrium conditions, predicted by the ThermoCalc software. The microstructure of René 108 was mainly dual-phase, γ and γ' in its initial state, with the γ' precipitates being the predominate phase. A temperature increase led to a gradual decrease in γ' precipitate volume fraction. Above 1052 °C, the γ matrix began to dominate, while the γ' solvus temperature is 1281 °C. The predicted amount of MC carbides and M_5B_3 borides in the analysed temperature range is lower than 0.01. Upon reaching approx. 1282 °C, a strong decrease in MC carbide volume fraction was observed. Only after exceeding this temperature did intensive carbide dissolution takes place. The M_5B_3 borides were stable at intermediate temperatures,
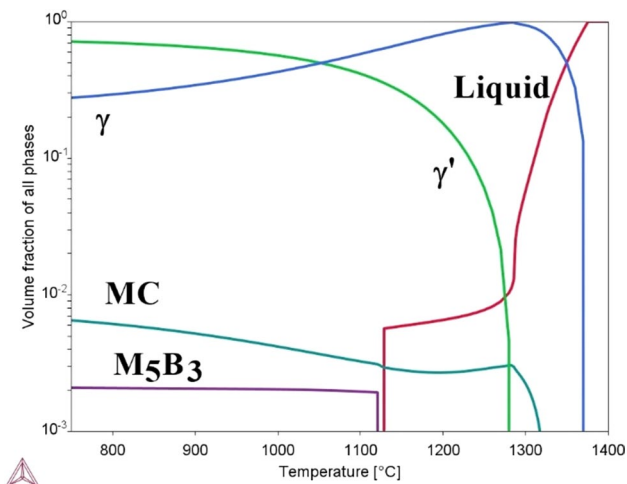
and their volume fraction in the microstructure almost did not change, while exceeding 1120 °C led to their rapid dissolution.

The DSC curve registered on-heating is presented in Fig. 3. The dominant strengthening phase was γ', which dissolves in a wide range of temperatures, however the maximum temperature for γ' dissolution was defined as 1228 °C. The MC carbides and M_5B_3 borides dissolved in the same range, however, due to their small volume fraction, the thermal effect coincided with the effect originating from the γ' phase. After exceeding 1294 °C, the liquid phase began to form, which is most likely due to the melting of the γ–γ' eutectic phase. Eutectic γ–γ' is not included in the ThermoCalc diagram as it is a non-equilibrium phase. The liquidus temperature was 1356 °C, and an endothermic effect of 60.7 J/g accompanied the phase transformation. Complete carbide dissolution most likely occurs after the liquid forms due to the presence of high melting point elements in René 108, such as Hf and Ta, which are widely known to be strong carbide formers. The liquidus temperature (T_L) determined via DSC was used in the hot ductility study.

The microstructure of René 108 in pre-weld state possesses a dendritic microstructure (Fig. 4). The features of
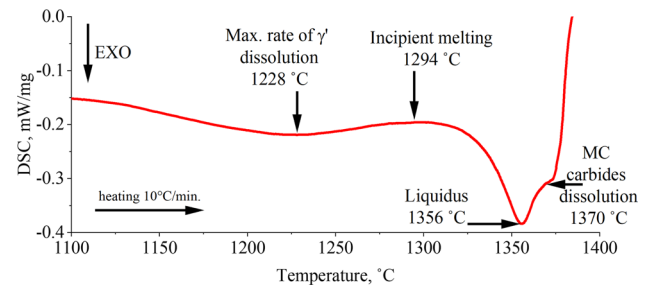

Fig. 3 DSC curve of the Rene 108 superally registered on heating

Fig. 2 Change in phase volume fraction as a function of temperature under equilibrium conditions
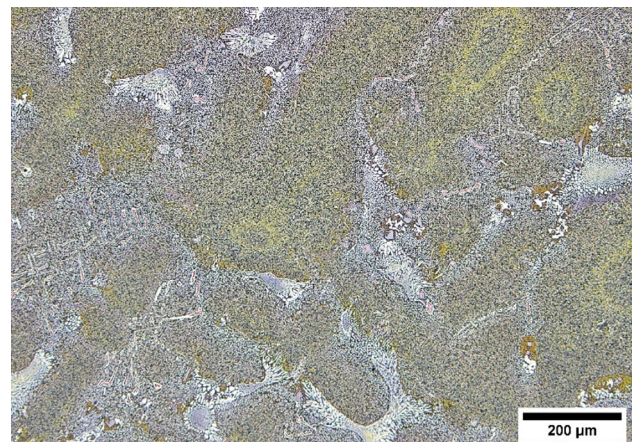

Fig. 4 Dendritic structure of cast fully heat-treated Renè 108 in pre-weld state, LM

the primary microstructure remained after complete heat treatment (solutionizing and ageing). The γ + γ' phase can be found in the dendritic regions, with additional inhomogeneously distributed eutectic γ–γ' islands and carbides being visible within the interdendritic spaces.

The dendritic regions revealed a relatively high volume fraction of approx. 55% secondary γ' precipitates, based on image analysis (Fig. 5), while the volume fraction of all γ' precipitates in René 108 was approx. 63% (estimated via XRD) [16]. These precipitates were characterised by a typical cube-shaped morphology. Larger secondary γ' exhibited a typical increasing degree of ageing. The morphology of the γ' precipitates depends on the local equilibrium conditions determined by the chemical composition, elastic stresses, and precipitate interactions. These factors change as a function of temperature and ageing time and are determined by the system's tendency to achieve thermodynamic equilibrium [17]. Within the matrix channels, numerous spherical-shaped tertiary γ' precipitates can be observed. Their morphology and location indicate that they were formed during cooling after ageing.

STEM investigations were performed to obtain more detailed information about the pre-weld microstructure (Fig. 6). The imaged γ/γ' interfaces at the atomic
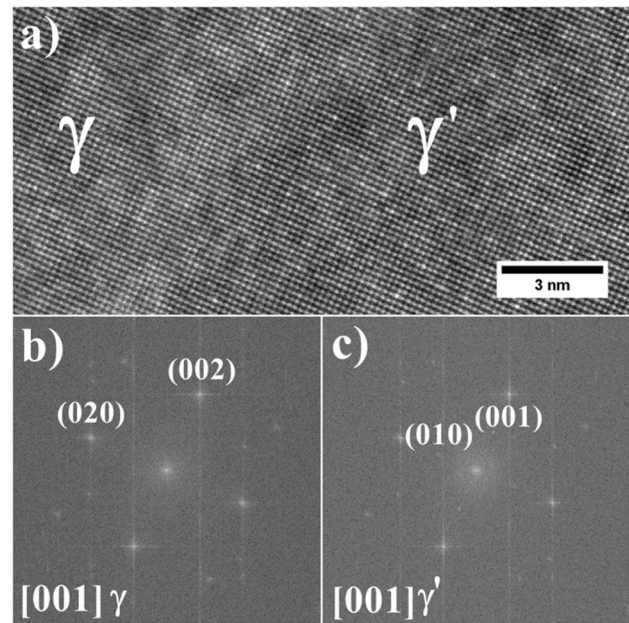

Fig. 6 **a** Interface of γ/γ', STEM-HAADF; **b**, **c** reflexes of the γ and γ' phases, FFT

scale were captured with an incident beam parallel to the < 001 > crystallographic orientation. The images

**Fig. 5** Morphology of γ' precipitates in the dendritic region: **a** Secondary precipitates; **b** Secondary and tertiary precipitates; **c** Histogram of the precipitates mean size with the log-normal distribution curve, SEM-BSE
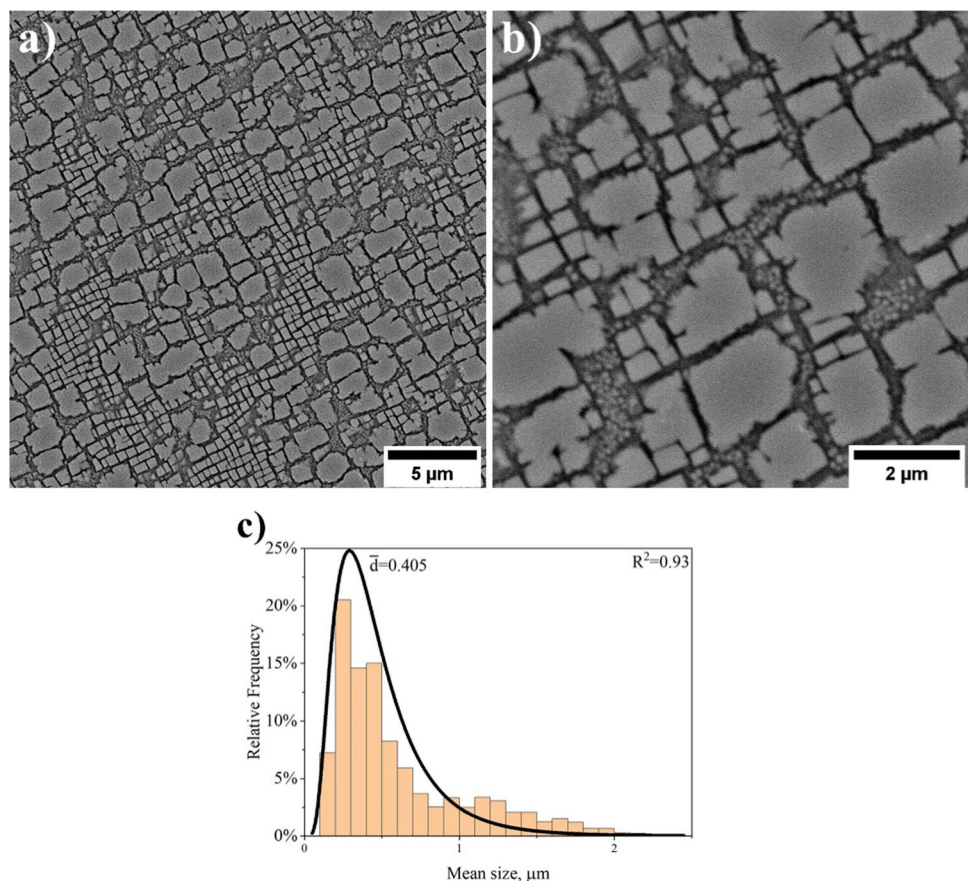
revealed that the interplanar distances for the γ matrix and coherent γ' precipitates are similar. The nanostructure was subjected to FFT to attain individual reflexes for the γ and γ' phases. Reflections {002}, {020} and {022} were obtained for the face-centred cubic (FCC) matrix, whereas for the ordered $L1_2$ structure of the γ' phase, additional {001}, {010} and {011} superlattice reflections were present. It is in line with the typical cube-cube orientation relationship, which can be described as: {100} γ//{100} γ'; <010> γ// <010> γ'.

The imaging of the γ/γ' interfaces via TEM-BF (bright field) revealed the presence of nanoprecipitates (Fig. 7a). On the LM and SEM-BSE images, these nanoprecipitates were not detected. High-resolution images of the nanoprecipitates at γ/γ' interfaces were used to calculate the FFT data (Fig. 7b,e). Based on the reflections, both nanoprecipitates were identified as M_5B_3 borides that crystallise in a body-centred cubic (BCC) crystal structure (D8$_1$-type structure-Strukturbericht notation) with nominal lattice parameters of a = 5,46 Å and c = 10,64 Å. The diamond-shaped borides are characterised by a crystallographic orientation relationship

Fig. 7 a M_5B_3 borides at γ/γ′ interfaces, TEM-BF; **b**, **d** diamond-shaped M_5B_3 boride oriented in the [3 $\overline{1}$ 0] zone axis; **c**, **e** polygonal-shaped M_5B_3 boride oriented in the [001] zone axis, STEM-HAADF
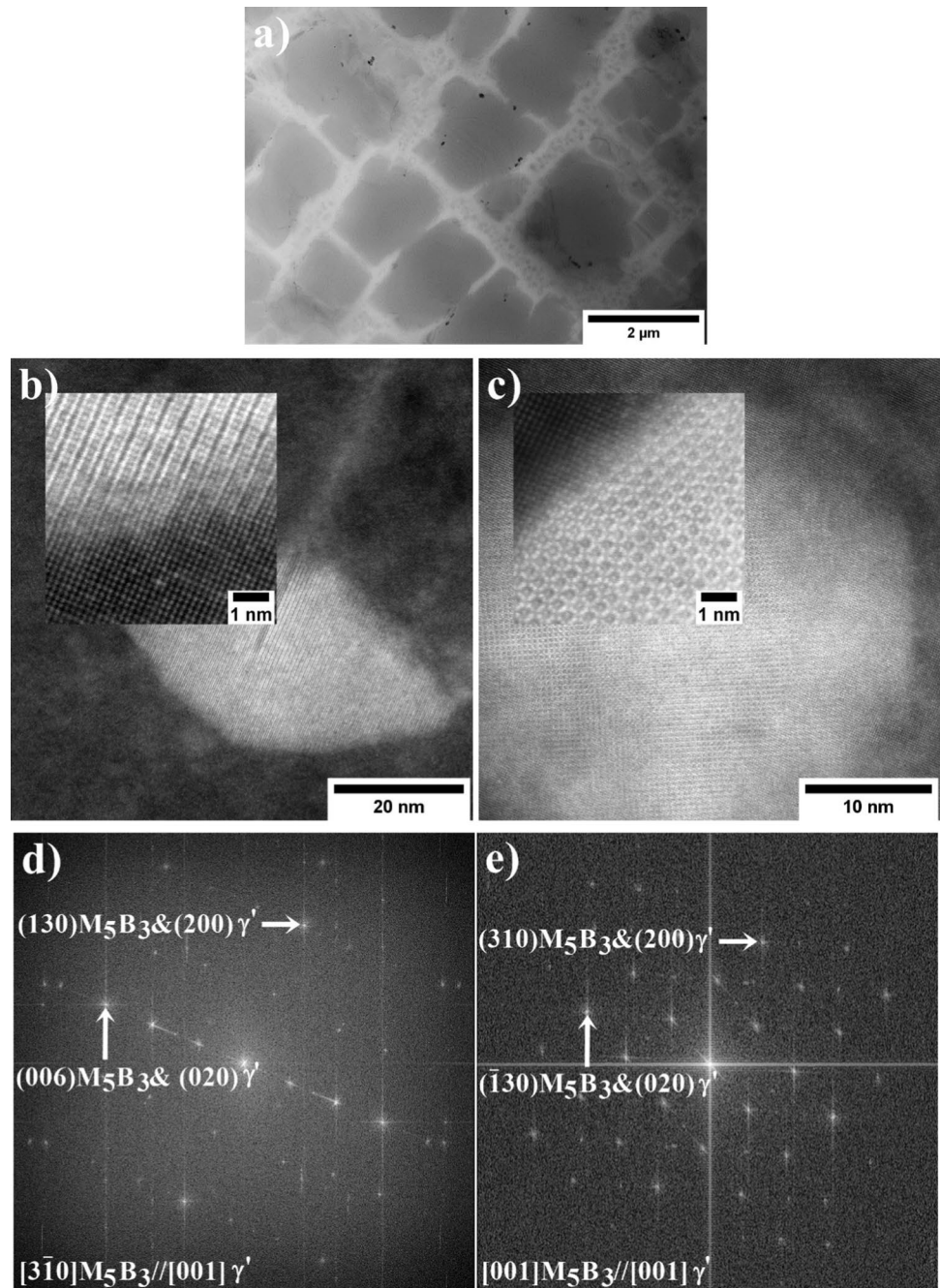
of $(130)_{M5B3}//(200)_{\gamma'}$; $[3\bar{1}0]_{M5B3}//[001]_{\gamma'}$ with the surrounding phase. The structure of a polygonal-shaped M_5B_3 nanoboride is shown along the four-fold [001] M_5B_3 direction. The image along the [001] zone axis displayed only one type of Wyckoff site. Due to the weak scattering ability of boron atoms, they were not seen in the STEM-HAADF images. The relationship between γ, γ' and the M_5B_3 phase is $[001]_{M5B3}//[001]_{\gamma'}$; $(310)_{M5B3}//(200)_{\gamma'}$. The boron atom is larger than the carbon and nitrogen atoms and smaller than the substitution atoms dissolved in the matrix (Co, Cr). It is energetically advantageous to segregate boron into areas with loosely packed atoms, like interfacial boundaries. Boron's solubility in FCC structures is very low. Goldschmidt [18] showed that at 1125 °C in austenitic steel (18% Cr, 15% Ni), the solubility of boron in the matrix is 97 ppm, while at 900 °C it is below 30 ppm.

At the grain boundaries, there are both continuous and discontinuous layers of bright precipitates (Fig. 8a). On the STEM-HAADF image, they are present as single diamond-shaped or polygonal precipitates (Fig. 8b). The STEM-EDX mapping shows strong enrichment in Cr and W (Fig. 8c). The selected STEM-HAADF image of the nanoprecipitate was subjected to a two-dimensional FFT to identify the crystallographic structure (Fig. 8d–e). The distribution of the dots in the FFT image corresponds to the M_5B_3 borides, similarly like on the γ/γ' interfaces.

The microstructure of the interdendritic regions is much more complex due to the additional presence of eutectic γ–γ' and carbides. The γ–γ' eutectic can possess a rosette-like morphology (Fig. 9a), while in other regions it can be less complex, and more rounded (Fig. 9b). The change in shape is affected by their irregular distribution along the interdendritic spaces. Non-equilibrium γ–γ' eutectic formation is caused by the micro-segregation of γ'-formers during casting solidification. This is detrimental from the point of view of welding due to the lowering of the incipient melting temperature.

Figure 10 shows the irregular distribution and various carbide morphologies. Their shape varies from fine blocks to complex Chinese script-like patterns. The location and morphology of the carbides indicates at which stage of casting solidification they were formed. The first to precipitate from the liquid are blocky-shaped carbides (under conditions close to equilibrium), whereas those with a more complex morphology (such as Chinese script) originate from the two-phase range: liquid + solid (mushy zone). Additionally, carbide morphology strongly depends also on the temperature
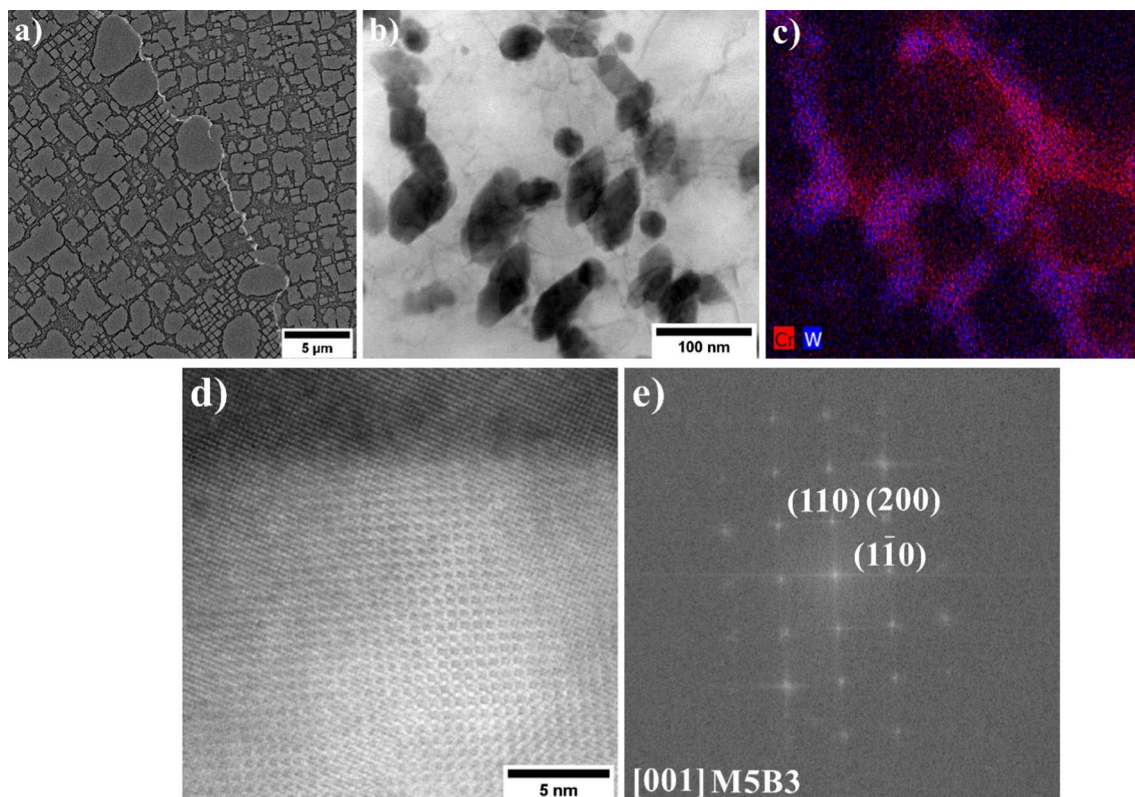

Fig. 8 **a** M_5B_3 precipitates along grain boundaries, SEM-BSE; **b**, **c** M_5B_3 precipitates morphology, Cr and W distribution, STEM-EDX; **d**, **e** M_5B_3 nanostructure and corresponding FFT, STEM-HAADF

Fig. 9 Morphology of the eutectic γ-γ' in the interdendritic region: **a** Rosette-like; **b** Rounded-like, SEM-BSE
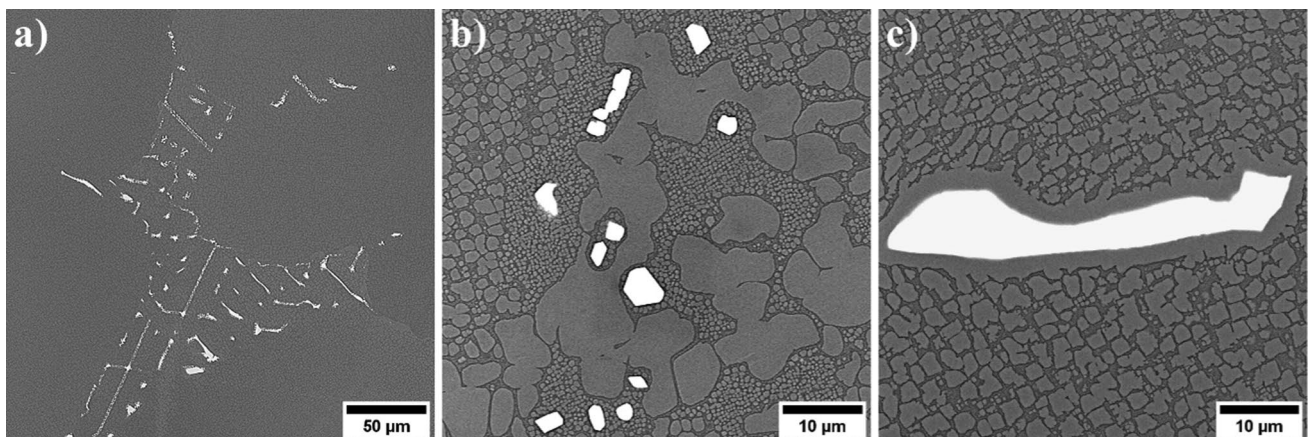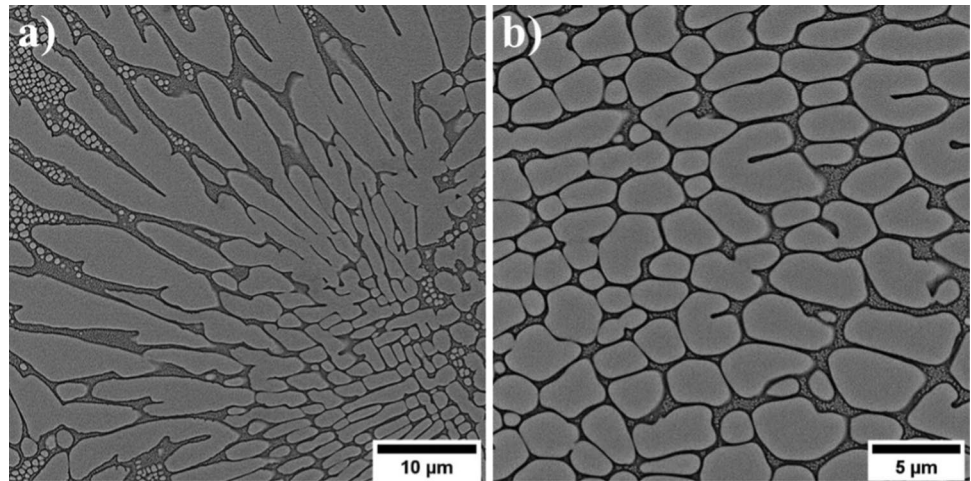

Fig. 10 Carbides morphology: **a** Chinese script; **b** blocky-shaped; **c** elongated block, SEM-BSE

gradient. The fine blocks that precipitated first are usually located inside or near the γ–γ' eutectic. As the temperature gradient decreases, the carbides become larger and take on more complex shapes. Carbide distribution and morphology are important microstructure features in the context of weldability as they can significantly reduce the hot ductility of the welded material (especially compact parallelogram-shaped carbides located along the grain boundaries).

Numerous carbide-forming elements exist in the René 108 superalloy, namely Hf, Ta, Ti, W, and Cr. In a selected carbide with a blocky-shaped morphology close to the γ-γ' eutectic island, the distribution of the alloying elements was analysed via STEM-EDX (Fig. 11). It can be seen that such carbides are characterised by an increased concentration of Hf, Ta, and Ti. However, semi-quantitative analysis results indicate that the dominant element is Hf.

MC carbides, mainly of the "Chinese script" type, also may possess a core–shell morphology with secondary γ' precipitates in interdendritic spaces. Those surrounding layers are about 1.0–1.5 μm thick. Based on FFT image analysis, it

is visible that MC carbides crystalised in the FCC (Fm-3 m) structure, with a nominal parameter a = 4.44 Å (TaC) or a = 4.64 Å (HfC) [19], and are non-coherent with the γ matrix. At the edges of large γ' precipitates surrounding the carbides, similarly to the dendritic regions, there are numerous M_5B_3 nanoprecipitates. However, borides did not occur at all interfaces of the cubic γ' precipitates with the matrix, as the boron concentration was not always high enough to facilitate formation of borides.

Despite the differences in morphology, almost all carbides are MC-type with an FCC structure. The exception is the $M_{23}C_6$ carbide detected on the edges of some MC carbides ones with Chinese script morphologies (Fig. 12d, e). To clearly identify chemical composition differences in this region, STEM-EDX mapping was performed in the area including secondary γ', MC and $M_{23}C_6$ carbides (Fig. 13). Within the mainly Ta-enriched region, Hf and Ti correspond to MC carbides, while the one enriched in Ni and A, to secondary γ'. Between these two phases, a nanolayer of $M_{23}C_6$, with an increased concentration of Cr was detected. The

Fig. 11 Distribution of the selected alloying elements in the interdendritic space, STEM-EDX
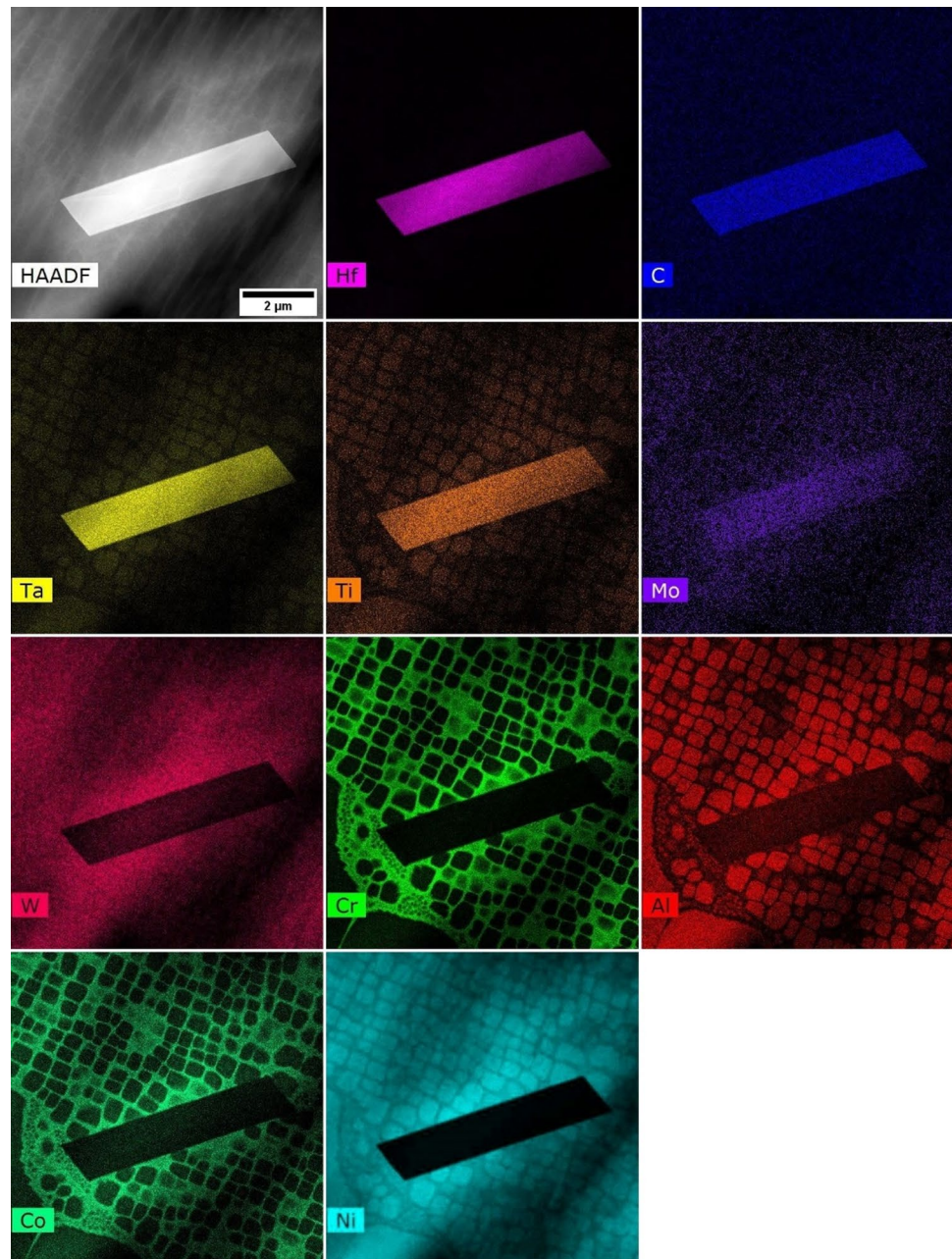
$M_{23}C_6$ carbide was only present on the edges of complex-shaped carbides surrounded by γ' (core–shell-like) and missing from the edges of blocky carbides near the γ–γ' eutectic. This indicates that stability differences between these specific carbides brought on the phase transformation widely known as $MC + γ → M_{23}C_6 + γ'$.

3.2 Hot ductility study

The high-temperature strength of Ni-based superalloys plays an important role in the accommodation of welding stresses [20]. Based on the hot ductility study, it is estimated that the nil strength of the René 108 superalloy is obtained at 1292 °C. The on-heating and on-cooling hot ductility were determined above 950 °C, with a heating rate of 150 °C/s. The ultimate tensile strength (UTS) values were found to be in the range of 950–1250 °C (Fig. 14a). Much higher stress values were obtained in samples broken on-heating. A decrease in the UTS value accompanied the increase in heating temperature. At 975 °C, the highest average value of 1107 MPa was obtained, while only 53 MPa was reached at 1250 °C (more than a 20-fold decrease). At 950 °C, the mean area reduction is around 6.6%, and it decreases to about 2% at temperatures above 1200 °C (Fig. 14b). Already stress
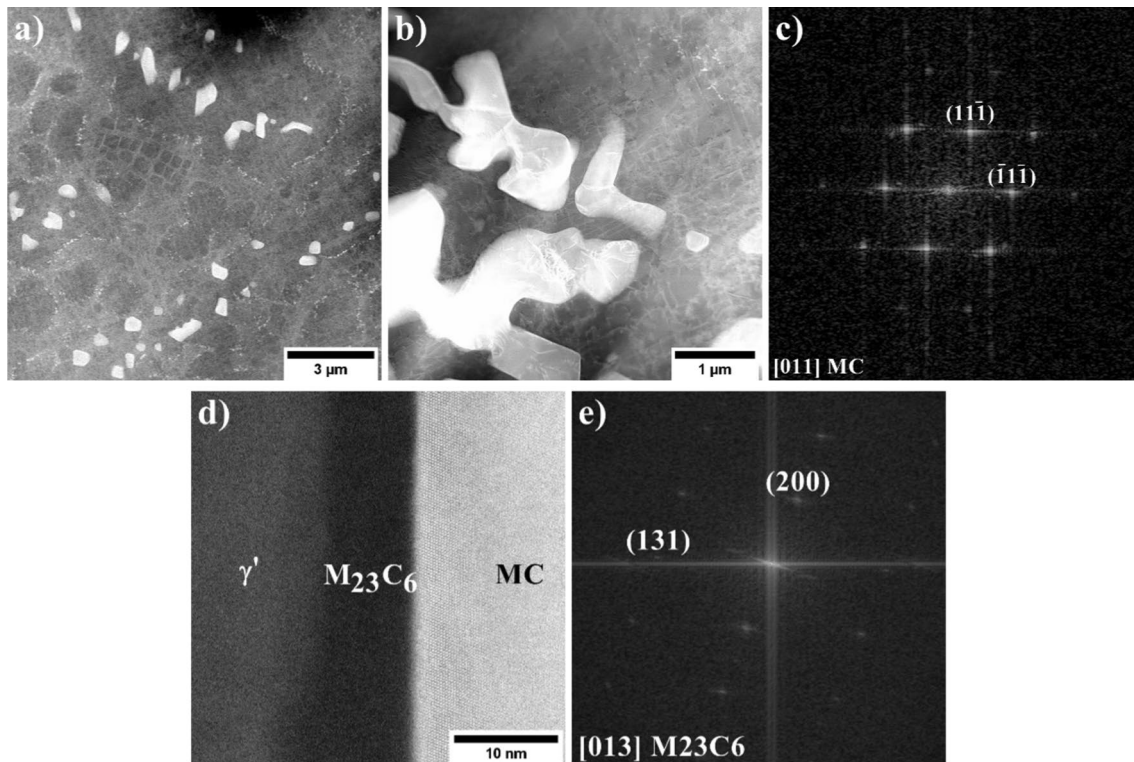
Fig. 12 **a** Core–shell morphology of MC carbides and γ' phase; **b** Morphology MC carbides inside the γ' precipitate; **c** SAED pattern of the MC carbide; **d** Interface $M_{23}C_6$/MC; **e** FFT image of the $M_{23}C_6$, STEM-HAADF

values below 200 MPa were enough to break the samples during on cooling from 1250 °C, indicating a substantial weakening of the material during pre-heating to 1250 °C. The recovery of plasticity temperature is determined when obtaining a reduction area of at least 5% during on-cooling testing, however, in the case of the René 108 superalloy, this was value was not reached. The highest reduction area measured for on-cooling samples was 2.9% at 1000 °C, with less than 2% reached for other temperatures. Therefore, the high-temperature brittleness range occurred at all tested temperatures, at which tests were performed. The hot ductility of René 108 was generally low and the rapid ductility decrease starting at 950 °C indicates early liquation onset in the material. While Ni-based superalloys are known to suffer from phase transformations that can locally supress the melting temperature and, in turn, affect weld cracking resistance, cast ATI 718Plus shows a comparatively high NDT of about 1160 °C [20]. Based on area reduction curve changes, the characteristic values are determined (Table 2). The ductility recovery rate (DRR), which is the difference between the maximum area reduction obtained during heating and the corresponding area reduction at that temperature during cooling, was 32.1%. The ratio of ductility recovery (RDR) was 36.2%. The obtained values are relatively low and indicate a potentially high susceptibility to hot cracking.

The hot cracking resistance of the René 108 superalloy was quantified using the $R_f = \frac{T_L - NST}{NST}$ coefficient. The T_L value is the liquidus temperature determined by DSC. An R_f equal to 0.05 suggests low resistance to hot cracking. For comparison, the Inconel 617 superalloy's R_f, characterised by better weldability, is equal to 0.13, which is typical for the entire group of Ni–Cr-Mo Ni-based alloys [21].

3.3 Microstructural changes induced by GTAW process

Prior to bead-on-plate specimen characterisation and weldability considerations, it is necessary to conduct a comprehensive analysis of the base material in pre-weld state. Once cracks are present in the welded sample, it is impossible to detect subtle changes or the presence of nanoparticles, due to their dissolution or vanishing caused by cavity formation. During welding, a high amount of heat is introduced into the material within a relatively short period of time. This can affect the precipitates strengthening René 108, which are characterised by various volume fractions, chemical compositions and stabilities. Figure 15 shows three distinct areas of a bead-on-plate sample's macrostructure, i.e. the melted region, a separating fusion line from the HAZ, and the base material. The most significant microstructural changes from

Fig. 13 Distribution of selected alloying elements in an area including secondary γ', MC and $M_{23}C_6$ carbides, STEM-EDX
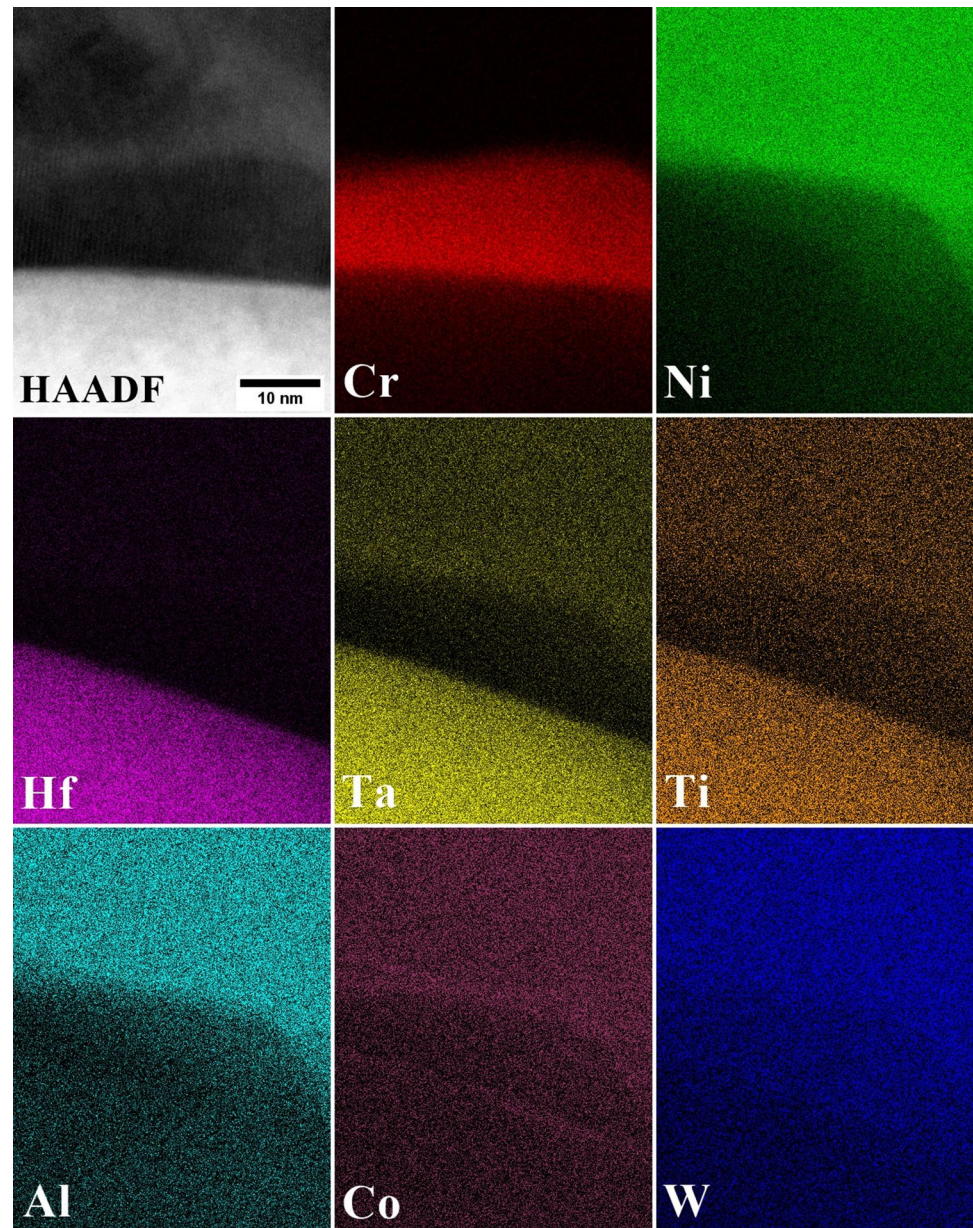
the superalloys' weldability point of view take place in the HAZ, so further observations were mainly carried out there.

Microstructural changes in the HAZ in dendritic regions and interdendritic spaces are shown in Fig. 16. It was observed that the dissolution of the γ' phase in and between the dendritic cores does not proceed identically. Differences in microstructural changes observed on the HAZ's cross-section result from casting heterogeneities and the distance between the HAZ and the fusion line (Fig. 16a). In HAZ areas, where the local temperature exceeded the γ' solvus (below bulk solidus temperature), the precipitates intensively dissolved (Fig. 16b). More intensive dissolution occurred in dendritic regions, where some of the γ' precipitates completely dissolved. Such

differences in dissolution kinetics of the γ' phase precipitates between dendritic regions and interdendritic spaces may result from the initial size of the precipitates, stress state and chemical composition variations. Secondary γ' precipitates in interdendritic spaces were larger, so the time needed for their substantial dissolution was longer. In turn, differences in the chemical composition of the γ' precipitates may affect the local change in their solvus temperature. The observed morphology indicates that it may be slightly higher for the secondary γ' precipitates in the interdendritic spaces. Chemical composition differences of the γ' in René 108 has been previously reported [17]. Ojo [22] showed that alloying element segregation, particularly Ti, into interdendritic spaces, led to higher γ'
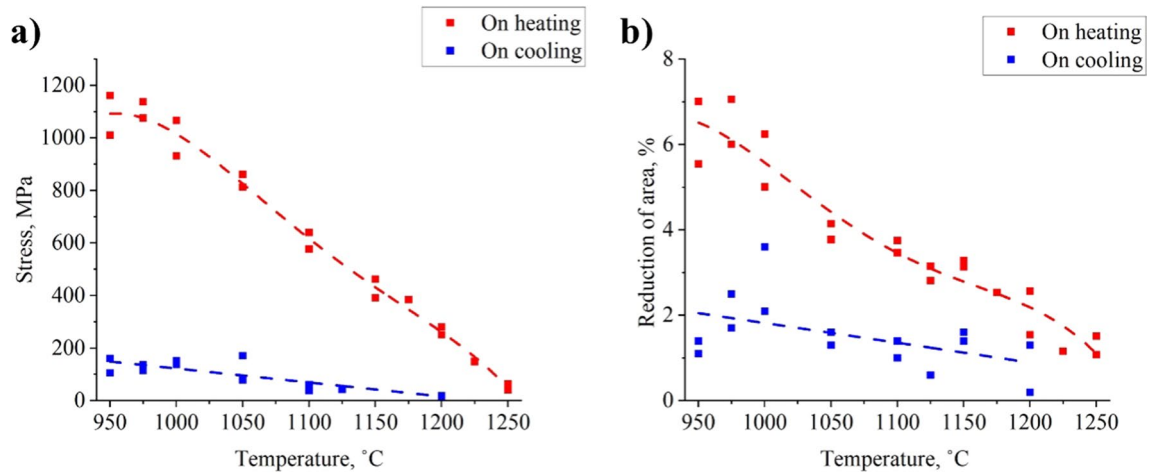
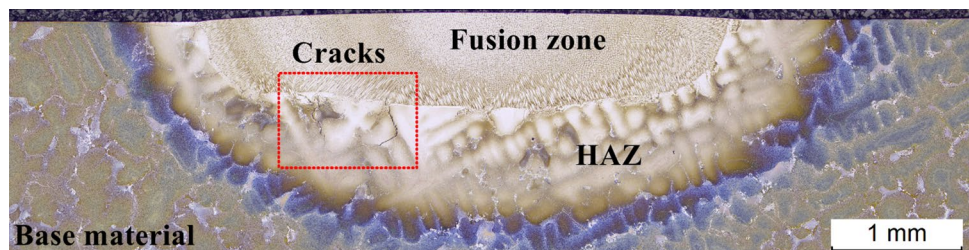**Fig. 14 a** Maximum force needed to rupture the samples; **b** mean area reduction

Table 2 Hot ductility parameters determined by Gleeble testing

Parameter	Unit	Value
Nil Strength Temperature, NST	°C	1292
Peak temperature (NST-40 °C)		1250
Nil Ductility Temperature, NDT		1225
Ductility Recovery Rate, DRR	%	32.1
Ratio of Ductility Recovery, RDR		36.2
Resistance to hot cracking, R_f	–	0.05

solvus temperatures and, in turn, larger precipitate sizes after continuous cooling compared to γ' precipitates in the dendritic regions. Rosenthal [23] stated that the solvus temperatures of interdendritic and core γ' precipitates in Inconel 738 can be at around 1170 °C and 1120 °C, respectively. As the distance from the fusion line in René 108 increases, the microstructural changes related to γ' precipitate partial dissolution are less intensive, mainly due to the lower temperature that is experienced during the GTAW process in this region (Fig. 16c, d).

The crack formation area (Fig. 17), shows the presence of both solidification (area 1) and liquation (area 2) cracking. The solidification crack (approx. 50 μm in length) originating from the fusion zone did not propagate towards the HAZ, running instead along a crystallite boundary.

Longer cracks orientated perpendicular to the fusion line reach the HAZ, therefore this area was studied in more detail.

Liquation cracking was initiated near a eutectic γ–γ' island. A thicker layer of structural constituents, formed during the re-solidification of the liquated region, can be found locally at the edges of the crack. More liquid formed through constitutional liquation and spread along the boundaries. This could be favoured by the segregation of alloying elements near the eutectic γ–γ' islands, which resulted in a local deviation in solidus temperature. As a result of high amounts of liquid stored in crack-free regions solidifying through migration, so-called liquid film migration (LFM) zones formed (Fig. 18).

Their presence may lead to crack gap width reduction or indeed complete microcrack self-healing. Their influence was observed by following the liquation crack (Fig. 19), where two large LFM zones were present. The first LFM zone, found approximately 100 μm from the fusion line, did not prevent the crack gap from opening. The second one, which formed deeper (about 150 μm), locally stopped the propagating crack. The crack also coursed along the edges of the large secondary γ' precipitates and MC carbides. As the distance from the fusion line increased, the crack gap narrowed, and was finally stopped at a depth of about 350 μm.
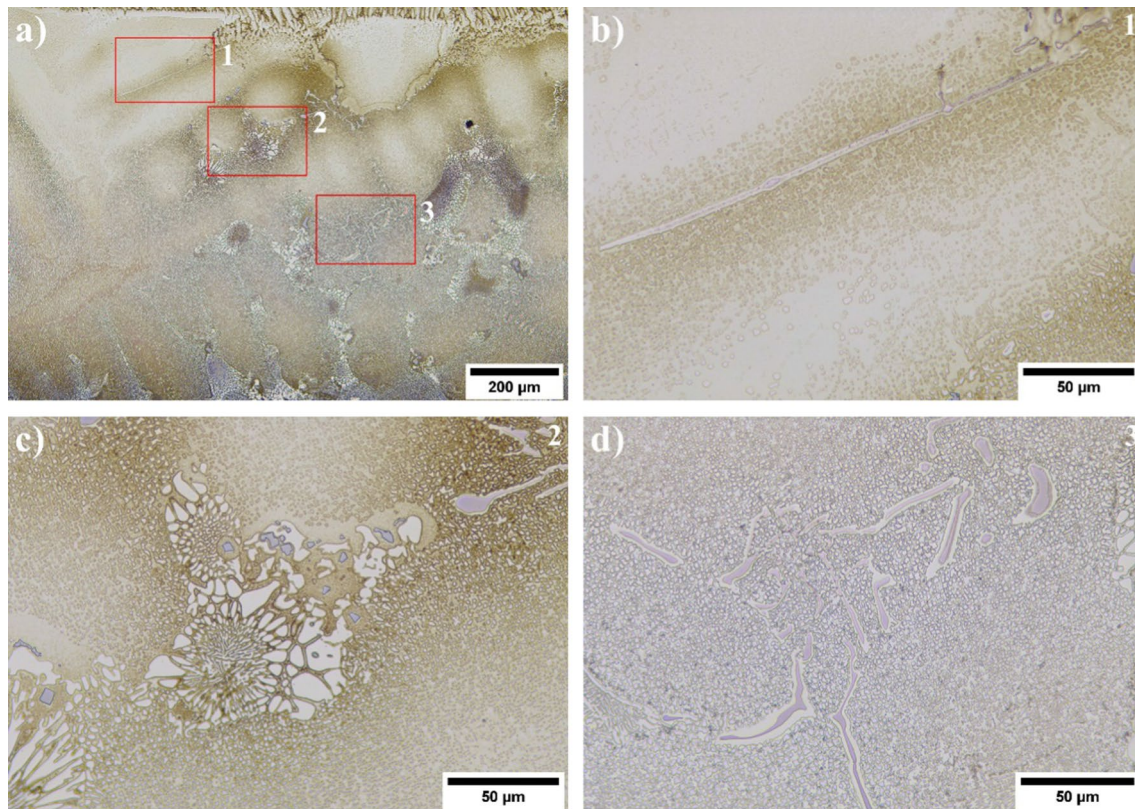
Fig. 15 Cross-sectioned bead-on-plate macrostructure of the René 108, LM

Fig. 16 Microstructural changes in crack-free regions of the HAZ: **a** location of regions 1–3; **b** differences in precipitate dissolution behaviour within dendrites and interdendritic spaces; **c** partial precipitate dissolution at around 250 µm from fusion line; **d** carbides surrounded by γ' precipitates around 500 µm from fusion line, LM
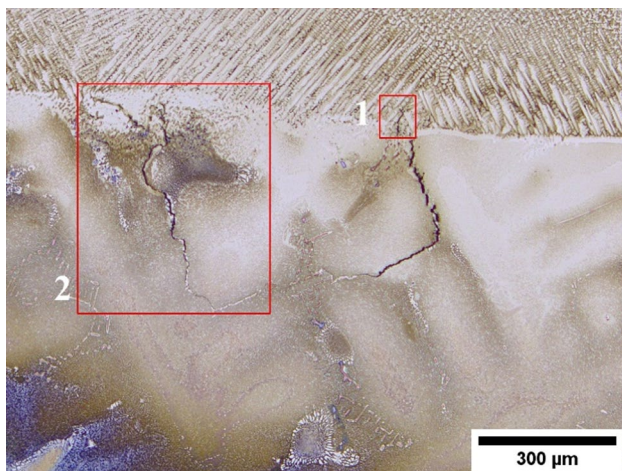

Fig. 17 Cracks locations induced by GTAW in the René 108, LM

The morphology of the precipitates near the liquation cracks was subjected to more detailed observations via SEM (Fig. 20). The HAZ cracks were intergranular with a relatively irregular zigzag morphology, typical for liquation cracks. The formation of the liquid during welding may be related to the eutectic γ–γ' phase or constitutional liquation of second-phase precipitates. The mechanism behind liquid crystallisation at the edges of the crack (illustrated by the morphology of the solidifying liquid layer) may provide an explanation for its formation. At the crack edges (Fig. 20b, c, area (1), a thick layer of re-solidification products, constituting a fine γ–γ' eutectic, can be seen, indicating highly intense constitutional liquation. This effect was promoted by its close proximity to the fusion zone, where the temperature was the highest. The crack also formed in the vicinity of morphologically complex carbides (Fig. 20d–f, area (2). Based on the pre-welding base material study, it was shown that these carbides are surrounded by γ' precipitates and formed a "core–shell" morphology. The crack (induced by welding) created a cavity at the γ' precipitate/MC carbide interface, followed by a change in γ' precipitate morphology at its ages caused by constitutional liquation. The γ phase must be present to initiate $\gamma + \gamma' \rightarrow L$ phase transformation leading to the formation of a liquid. $M_{23}C_6 + \gamma' \rightarrow MC + \gamma$ phase transformation could occur during heating prior to constitutional liquation. Another option is the formation of a metastable γ phase film during welding, as a result of the γ' phase order→disorder transformation at the interface of
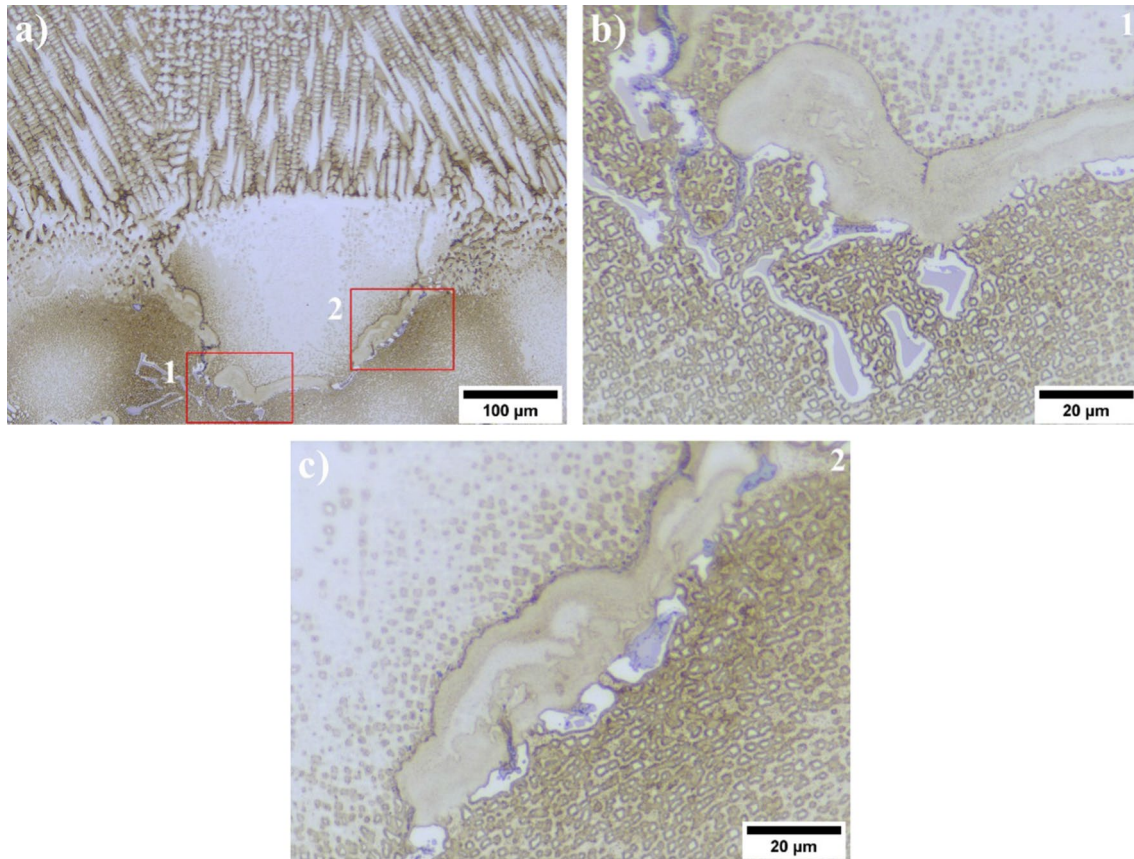
Fig. 18 a Location of the liquid film migration zones in HAZ; **b**, **c** Morphology of the liquid film migration zones, LM

the γ' precipitate. Liquid formation and this eutectic-type solidification is visible at the cavity's edge. In some regions, the amount of solidifying eutectic is relatively high, while in others it is difficult to observe. The high thermal stresses that accompany welding were the source of numerous secondary cracks inside the carbides. Secondary cracks, not preceded by plastic deformation, are brittle. Carbide edges in direct contact with the liquid phase during welding have very smooth surfaces, with the eutectic liquid probably not sufficiently wetting them. During welding, the carbides could be dissolved by diffusion. Considering the high stability of MC carbides, it can be stated that their participation in the initiation of constitutional liquation was probably negligible. Insufficient plastic deformation of the base material at elevated temperatures and the lack of sufficient amounts of liquid in regions far away from the fusion line lead to decohesion at the solid–liquid interface and then gradual stopping of crack development (Fig. 20g–h, area (3). This proves that all strengthening phases could participate in non-equilibrium liquid formation in René 108 and should be considered when discussing crack initiation mechanisms.

Sponseller [24], based on differential thermal analysis of Ni-based superalloys, stated that complete γ' phase

precipitate dissolution (without the risk of constitutional liquation) is possible when the heating rate is 0.03–0.16 °C/s. Ojo [25] confirmed that during Inconel 738LC superalloy arc welding, the heating rate is usually around 150 °C/s. Large secondary γ' precipitates under these heating conditions are stable up to about 1200 °C, after which they undergo constitutional liquation. With such rapid heating, like during welding or cladding, i.e. when deviating from equilibrium conditions, avoiding constitutional liquation appears to be challenging. The obtained results are in line with those published by Ojo [26], who investigated the Inconel 738LC Ni-based superalloy via Gleeble testing at four temperatures: 1140 °C, 1165 °C, 1180 °C, and 1245 °C (heating rate: 150 °C/s). The microstructural changes in the simulated HAZ indicated the initial constitutional liquation stage to start at 1165 °C. In on-heating samples broken at two subsequent temperatures, numerous precipitates with a γ–γ' eutectic morphology were revealed.

Crystallographic orientation studies of areas containing liquation cracks are shown in Fig. 21. Intergranular cracks are observed to propagate along high-angle grain boundaries. No differences between the γ and γ' phases were seen on the orientation maps, as the precipitates are coherent with
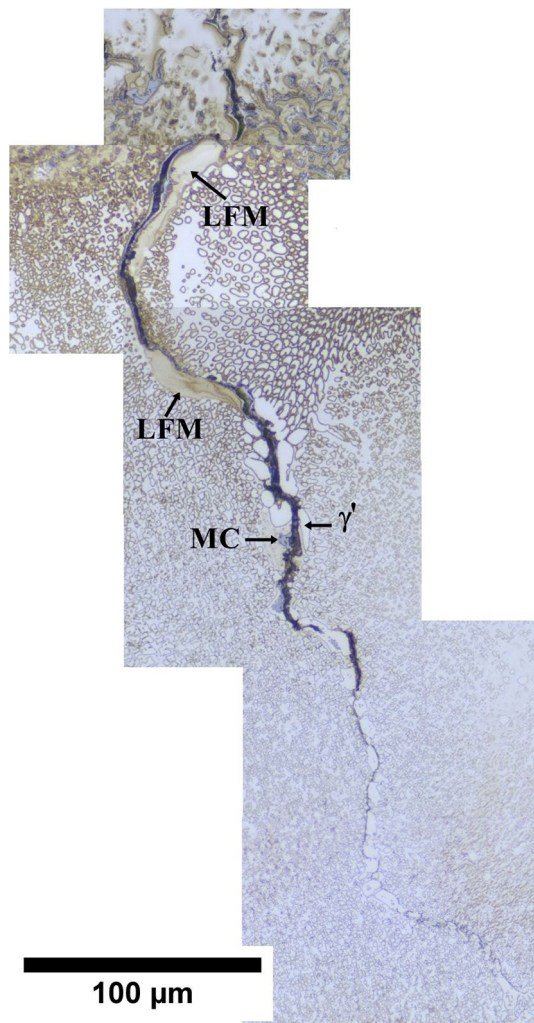
Fig. 19 Liquation crack morphology in area 2, LM

the matrix (confirmed via STEM). However, clear orientation differences were observed between the MC carbides and the two-phase area ($\gamma + \gamma'$), with the carbides playing a negligible role in non-equilibrium liquid film formation. The re-solidification products' morphology (Fig. 20) is typical for the γ–γ' eutectic. The EBSD images show that they nucleated epitaxially at the partially melted grain edges and grew in the favoured $< 001 >$ crystallographic direction. No change in the orientation of the resulting products confirms that it is the γ–γ' eutectic, and the dominant phase that experienced the non-equilibrium melting reaction was γ'.

MC carbides' influence of increasing liquation crack susceptibility in the René 108 superalloy is most likely related to their morphology and chemical composition. Kotval [27], based on an investigation of the influence of Hf on MC carbide morphology, showed that a 1.5 wt.%. addition of Hf has a positive effect on the fracture toughness of the MAR-M004 superalloy (modification of Alloy 713LC). MC carbides with

a "Chinese script" morphology, and especially those consisting of solid parallelogram-shaped cores and side arms, significantly reduce the superalloy's ductility. Cracks can easily propagate along their edges under the influence of welding stresses. Modifying the carbides' chemical composition by adding Hf significantly changes their morphology, with fine blocky-shaped carbides dominating. Therefore, the number of potential crack initiation points is reduced, in turn increasing the ductility and creep resistance of the superalloy. The unfavourable influence of the "Chinese script" carbides on the fracture toughness was also revealed in the GTA-welded MAR-M247 Ni-based superalloy [7]. There were numerous cracks in the carbides, which formed a local structural notch by strengthening the grain boundaries. Such cracks were not observed on blocky-shaped fine (Hf, Ta) C carbides. This is consistent with our observations on René 108. Ojo [28], for weldability evaluation of superalloys, divided carbides into two groups: low-temperature and high-temperature. Low-temperature carbides contain significant amounts of Nb and Zr. They are characterised by a high tendency to constitutional liquation during welding. The second group includes Ta-rich carbides, with a low tendency to constitutional liquation. When Inconel 738LC superalloy is heated up to liquidus temperature (about 1332 °C), the shape of these carbides changes slightly due to dissolution or liquation. Similar conclusions were formed by Baeslack [29], based on weldability tests of the Inconel 718 superalloy with a standard chemical composition, as well as a modified one (Ta replaced Nb). The Ta-alloyed variant was strengthened by TaC carbides, which are less prone to constitutional liquation compared to the less stable Nb-rich carbides. This is related to the temperature of eutectic transformation, which decreases in the following order Ni-Ta → Ni-Nb → Ni-Zr. Tantalum and hafnium carbides are the dominant species in the René 108 superalloy and are characterised by the highest melting point of all MC carbides (3880 °C and 3900 °C) and low chemical reactivity [30]. The second type of carbides observed in the René 108 superalloy are $M_{23}C_6$ carbides. These carbides are metastable and above 1010–1040 °C are completely dissolved in the γ matrix [31]. During René 108 superalloy welding, the temperature near the fusion line significantly exceeds these values, enabling $M_{23}C_6$ nano-precipitates, especially since local melting occurred there. Sims [2], however, confirmed that the $M_{23}C_6 + \gamma' \rightarrow MC + \gamma$ phase transformation can take place at high temperatures. The presence of the γ phase in the microstructure favours the constitutional liquation of γ' precipitates surrounding these carbides. The formation of a non-equilibrium liquid film may therefore also be favoured by other factors, apart from γ' phase precipitate liquation. Li [32] observed the first signs of constitutional liquation in the Inconel 617B superalloy at 1250 °C, while the solidus temperature was 1368 °C. Partially dissolved $M_{23}C_6$ carbides were the phase's response to

Fig. 20 Liquation cracking in the HAZ: **a** General view, **b**, **c** Re-solidification products on crack edges in area 1, **d**–**f** Carbide morphology on the crack edges in area 2, **g**–**h** Gradual stopping of crack propagation in area 3, SEM-BSE
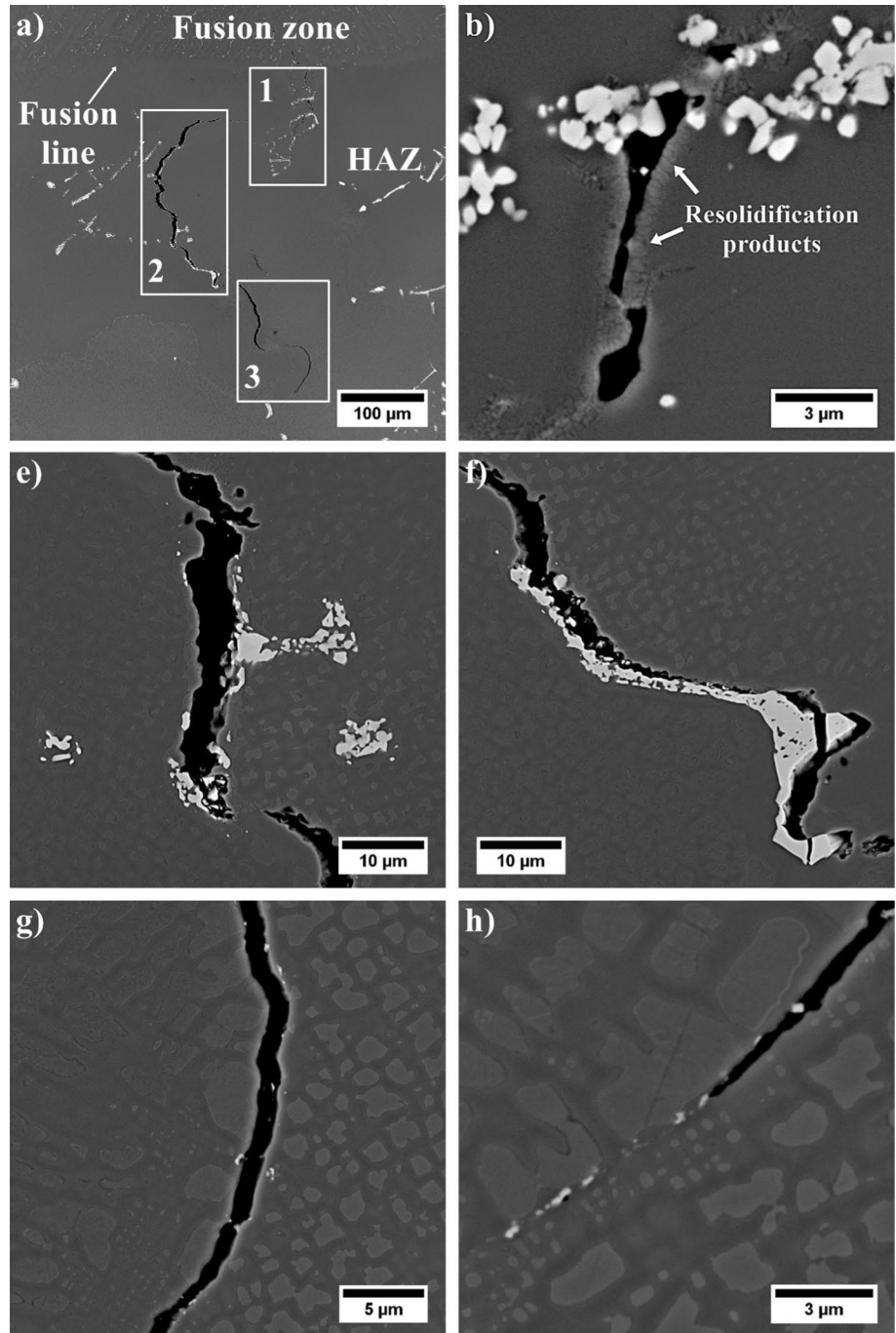

non-equilibrium liquid formation. Despite the constitutional liquation of $M_{23}C_6$ carbides during GTAW, liquation cracks did not appear in the microstructure.

Cracks also formed at grain boundaries without large MC carbides with the previously-described coarse-grained γ' core–shell morphology (Fig. 22a, b). The pre-weld state analysis and post-weld crack propagation analysis suggests that M_5B_3 borides also participated in phase transformation during welding. Additionally, variously-sized single cracks were identified. The precipitates' morphology at crack edges

indicates that a relatively low amount of liquid was present during the welding process. The liquid only partially wetted the melted grains and spread along their boundaries, without filling the cavities. The temperature increase within the HAZ induced by the welding led to a local increase in volume. During solidification, the first products of eutectic transformation crystallising on opposite crack edges are close to each other and the remaining space is filled with liquid. Stresses resulting from non-uniform shrinkage cause liquid film decohesion, which in turn leads to gap formation. In the

Fig. 21 Inverse pole figure maps (IPF-Z) of the region including liquation cracks, **a**–**d** Regions of cracks with MC carbides at the edge; **e** Orientation triangle, SEM-EBSD
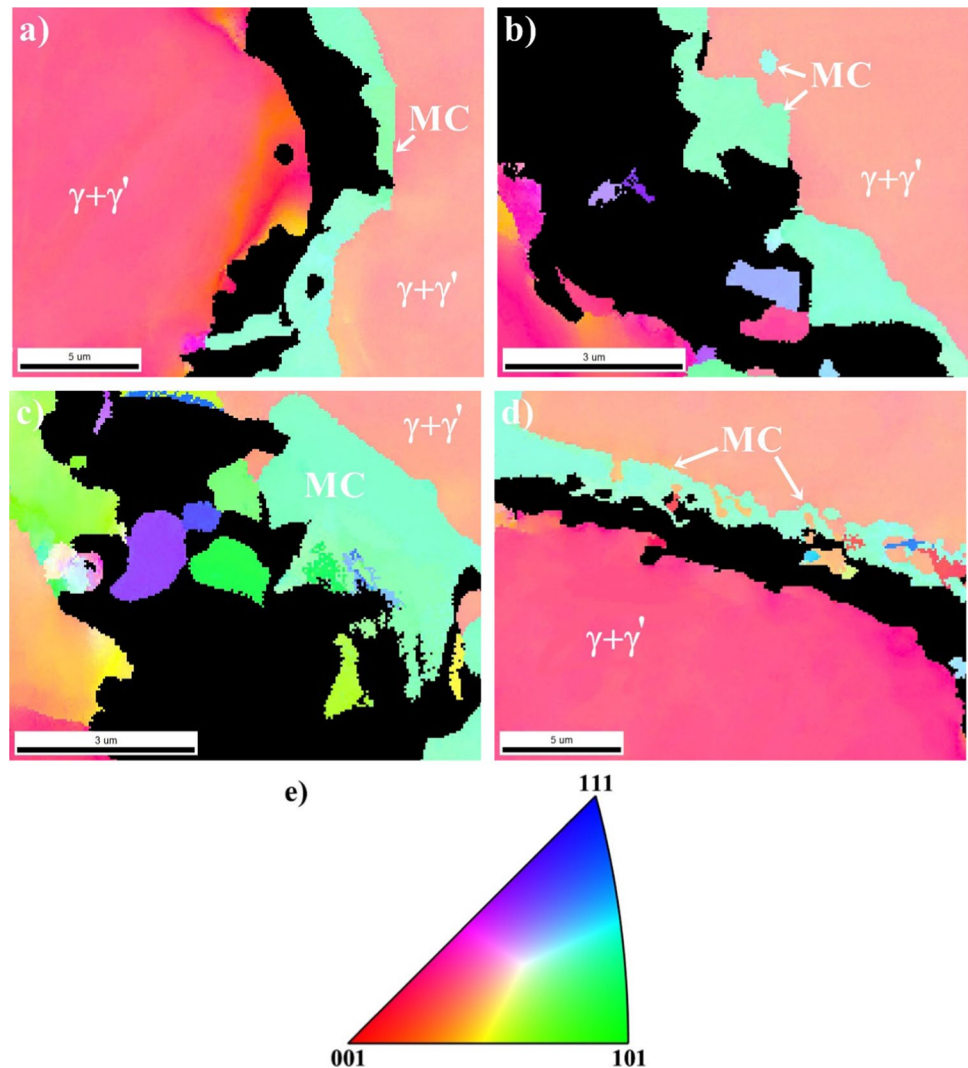
case when a relatively large volume of liquid is free to circulate, only slight microcracks remain in the microstructure. However, when γ–γ' eutectics growing epitaxially from two opposite grains come into contact, crack formation does not occur (Fig. 22c). The γ–γ' eutectics at the crack edges are characterised by a highly diverse morphology, which could result from chemical composition gradients, solidification rates, and locally varying liquid volume. In the presented examples, the γ' precipitates inside the grains close to the liquated grain edges were fully dissolved in the matrix during welding, which led to strong supersaturation. Then, during cooling, the γ' phase re-precipitated in the form of nano-precipitates with a spherical morphology (Fig. 22d). Locally, their diameter did not exceed 35 nm, and with increasing distance from the melted edge, their size gradually increased.

The nano M_5B_3 borides are not visible in the orientation maps at the edges if the liquation cracks (Fig. 23). The absorption of surface-active elements, like boron, into intergranular liquid usually decreases the solid–liquid interfacial energy, significantly enhancing wetting properties [33]. Therefore, the effect of locally increasing boron concentrations promoting microfissuring leads to increased cracking susceptibility [34]. For a specified solid–liquid interfacial energy, the higher the grain-boundary energy, the higher the tendency for it to be wetted and penetrated by a liquid. Equiaxed Ni-based superalloys do not have a privileged crystallographic grain orientation. Randomly oriented wide-angle grain boundaries (WA GB) have higher energies than low-angle grain boundaries (LA GB), where liquation cracking was not observed.

The role of the M_5B_3 boride in the cracking of Renè 108 is connected with boron's nature. During rapid heating, M_5B_3 borides along the grain boundaries can dissolve and/or melt, thus increasing the boron concentration at the M_5B_3/γ interface. According to thermodynamical simulations, the solvus temperatures of M_5B_3 in René 108 is 1120 °C, which is 174 °C below the incipient melting registered by DSC. The enrichment of the matrix in boron is naturally associated
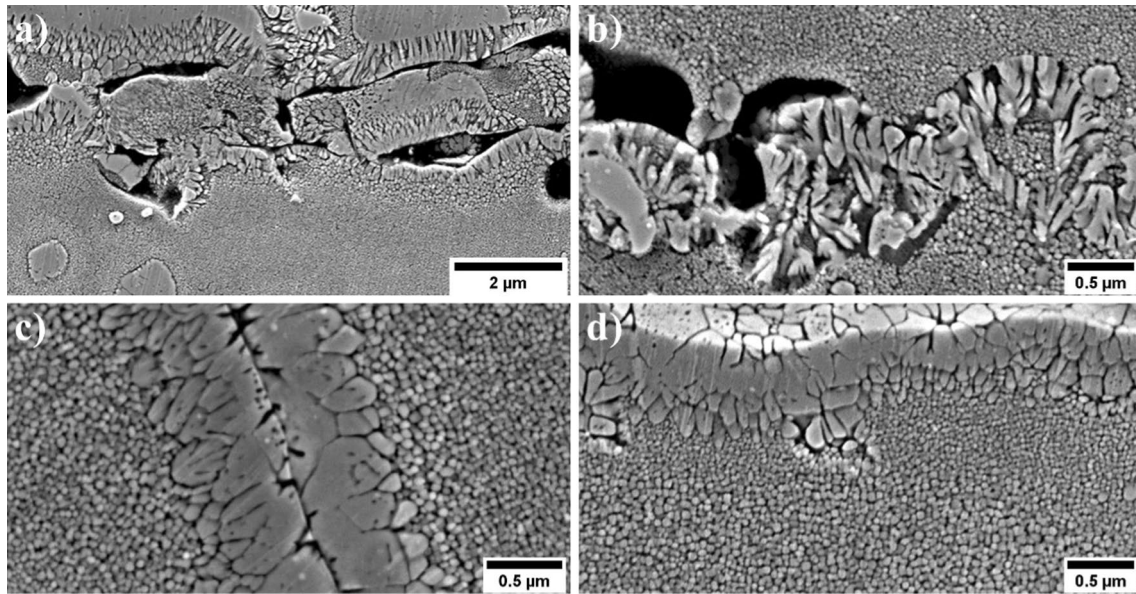
Fig. 22 Morphology of the re-solidification products: **a** Partially liquated large secondary γ'; **b** Micro-voids between re-solidification phases; **c** Local healing crack; **d** Size of γ' formed from the saturated matrix), SEM-SE

Fig. 23 Inverse pole figure maps (IPF-Z) of liquation cracks in a region without MC carbides on high-angle grain boundaries, **b** Lack of liquation cracking on low-angle grain boundaries, SEM-EBSD
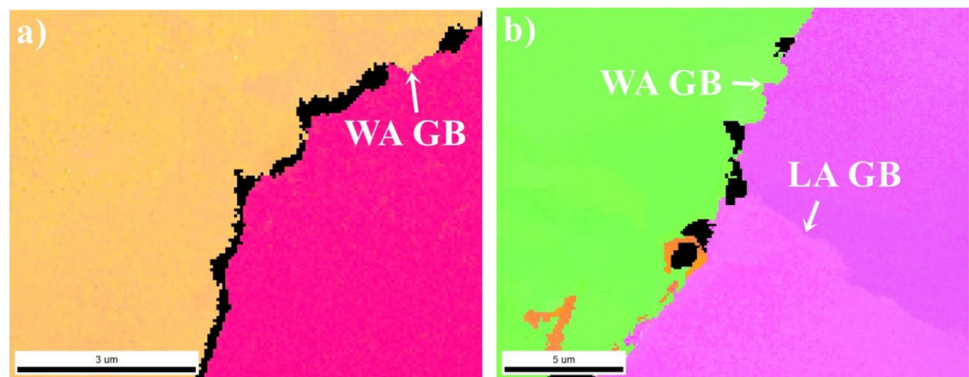
with a local decrease in melting point and subsequent broadening of the solidification temperature range. Therefore, B in the liquated grain boundaries leads to the liquid film being present at lower temperatures during cooling. There, tensile stresses accumulate and cause cracks to appear where the local strength was exceeded. Osoba [35], based on the Gleeble study of the Haynes 282 superalloy, showed that the M_5B_3 borides could also be liquated at 1150 °C and 1170 °C, while (Ti, Mo)C carbides were still stable. To reduce the susceptibility of Haynes 282 to liquation cracking, he proposed a pre-weld heat treatment in the range of 1080–1100 °C. The treatment led to M_5B_3 boride dissolution from the grain boundaries, contributing to improved weldability of the Haynes 282 superalloy.

Thin foils were prepared from areas containing γ–γ' re-solidification products at the grain boundaries and STEM-EDX was performed to image the distribution of alloying elements (Fig. 24). The elongated primary γ' precipitates

are divided by the matrix channel. Additionally, fine precipitates enriched in Ni and Al, typical for γ', were found locally in the γ matrix. A thin W-rich layer is observed along the primary γ' edges, which is probably connected with the dissolution of borides (rich in W), proving that M_5B_3 borides actively participate in liquation cracking. Tungsten is widely known to sluggishly diffuse, therefore the observed segregation can be linked to insufficient time for long-distance diffusion originating from a relatively high cooling rate, typical for welding processes.

The mere occurrence of constitutional liquation is not sufficient to make a superalloy's microstructure susceptible to cracking. For crack initiation, the liquid has to wet and spread along the grain-boundary regions to produce a continuous or semi-continuous intergranular film. Liquid film thickness and its temperature stability, at which sufficient thermal and mechanical stresses are generated on cooling, also strongly affect crack formation. Grain-boundary wetting
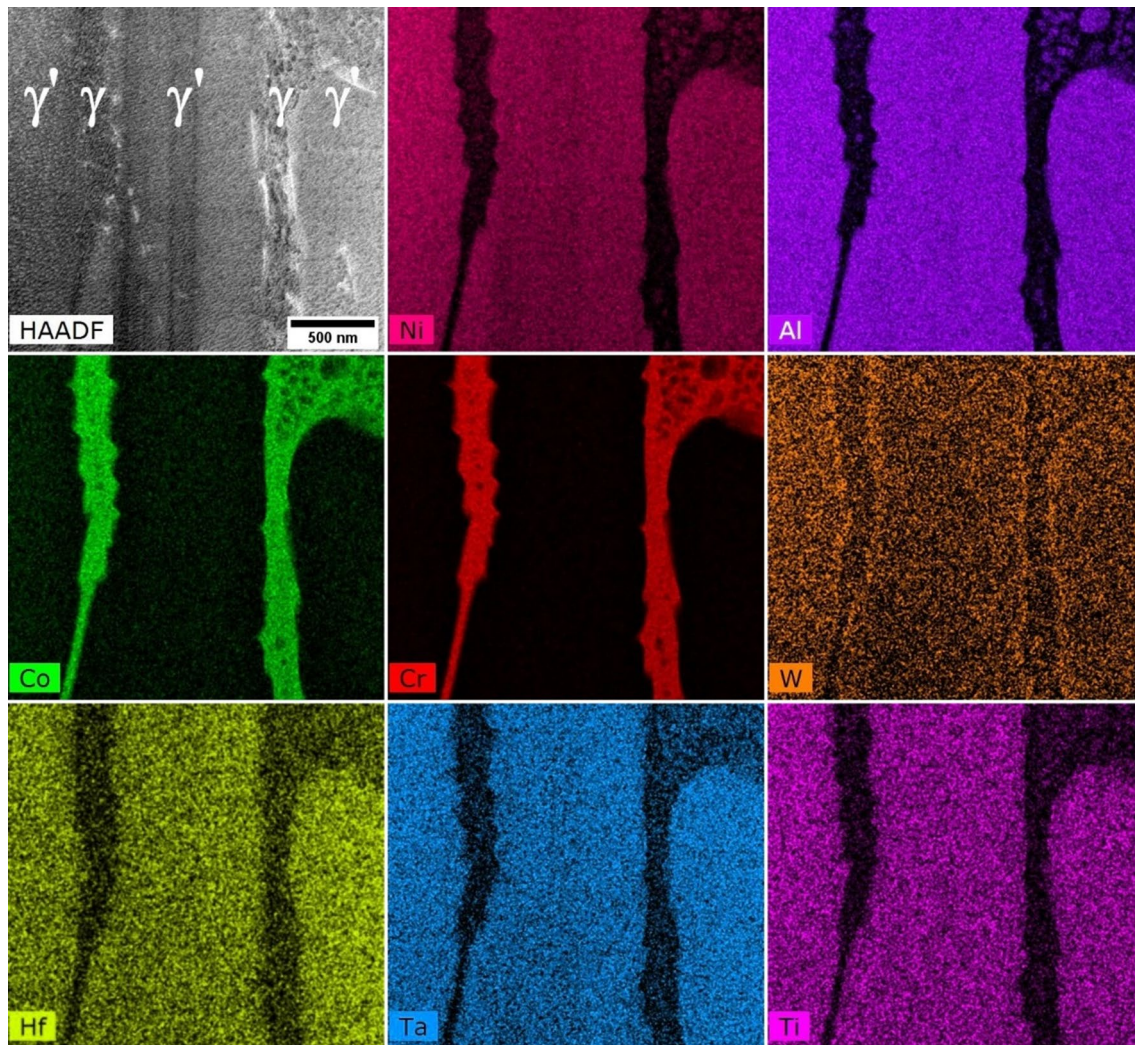
Fig. 24 Distribution of selected alloying elements in the re-solidification products formed along grain boundaries in the HAZ, STEM-EDX

can be increased if the solid–liquid interfacial energy is low compared to the grain-boundary energy. The grain boundaries can be completely, incompletely, or not wetted. Straumal [36] presented that in the first case, the grain boundary separating the grains is completely substituted by two solid–liquid interfaces. The contact angle between the grain boundary and the melt is then equal to zero. Wetting is incomplete when the grain boundary co-exists with the liquid phase, and the contact angle between GB and the melt is finite ($\theta > 0°$). A reversible transition from incomplete to complete wetting of grain boundaries could occur upon temperature increase, which could be considered as a surface phase transformation [37, 38].

The metastable liquid formed through constitutional liquation always reacts with the solid grain through solute back-diffusion, so the non-equilibrium solid–liquid interface energy is very low. Under such conditions, the extensive grain-boundary penetration and wetting by a film formed by constitutional liquation of γ' precipitates is expected. The microstructure indicates that the appearance of LFM in the HAZ is beneficial for enhancing liquation cracking in René 108 (Fig. 25). Two main driving forces affect LFM formation, namely the diffusional coherency strain energy and surface tension asymmetry at the two solid–liquid interfaces [39]. In the first one, considerable coherency strains originating from lattice mismatch will form if there are sufficient size differences between the diffusing solute in the metastable liquid and the matrix atoms. The second on requires a certain degree of curvature at the grain interfaces to create a considerable concentration gradient within the liquid and induce solute diffusive flux during the process. Grain-boundary curvature was recognised to be the main driving force of liquid film migration in the HAZ of Incoloy 903, which allowed to improve cracking resistance [40]. In the HAZ of the Inconel 738 superalloy, considerable LFM was found and explained by a serrated grain-boundary morphology [25].

Fig. 25 **a** Location of the LFM zone, **b** LFM zone and local crack self-healing, SEM-BSE
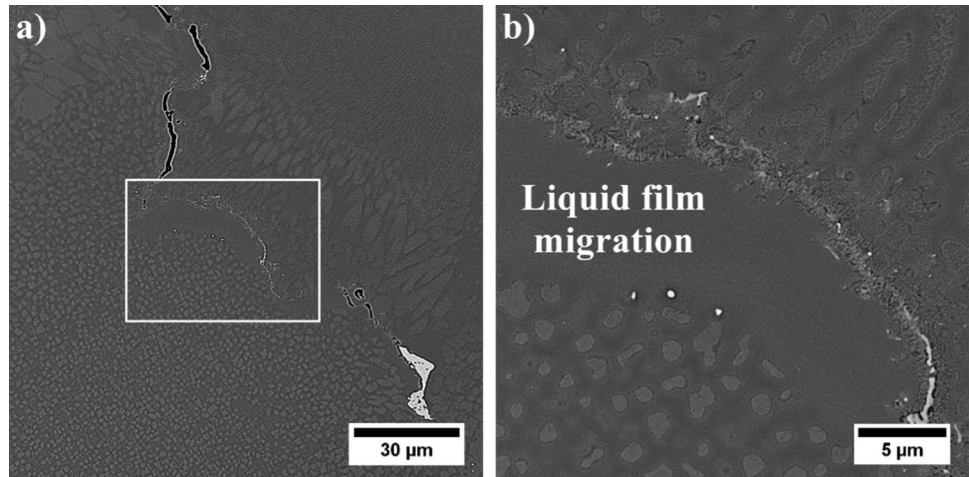
The formation of a thick liquid film may impede the effect of rapid re-solidification by LFM in preventing HAZ liquation cracking. The thick intergranular liquid film would not only prolong the time necessary for the entire liquid to disappear, but it could also reduce the driving force, with the increase in migration distances.

A characteristic feature of the crack fracture is its smooth surface, which proves that the solidifying liquid did not contact
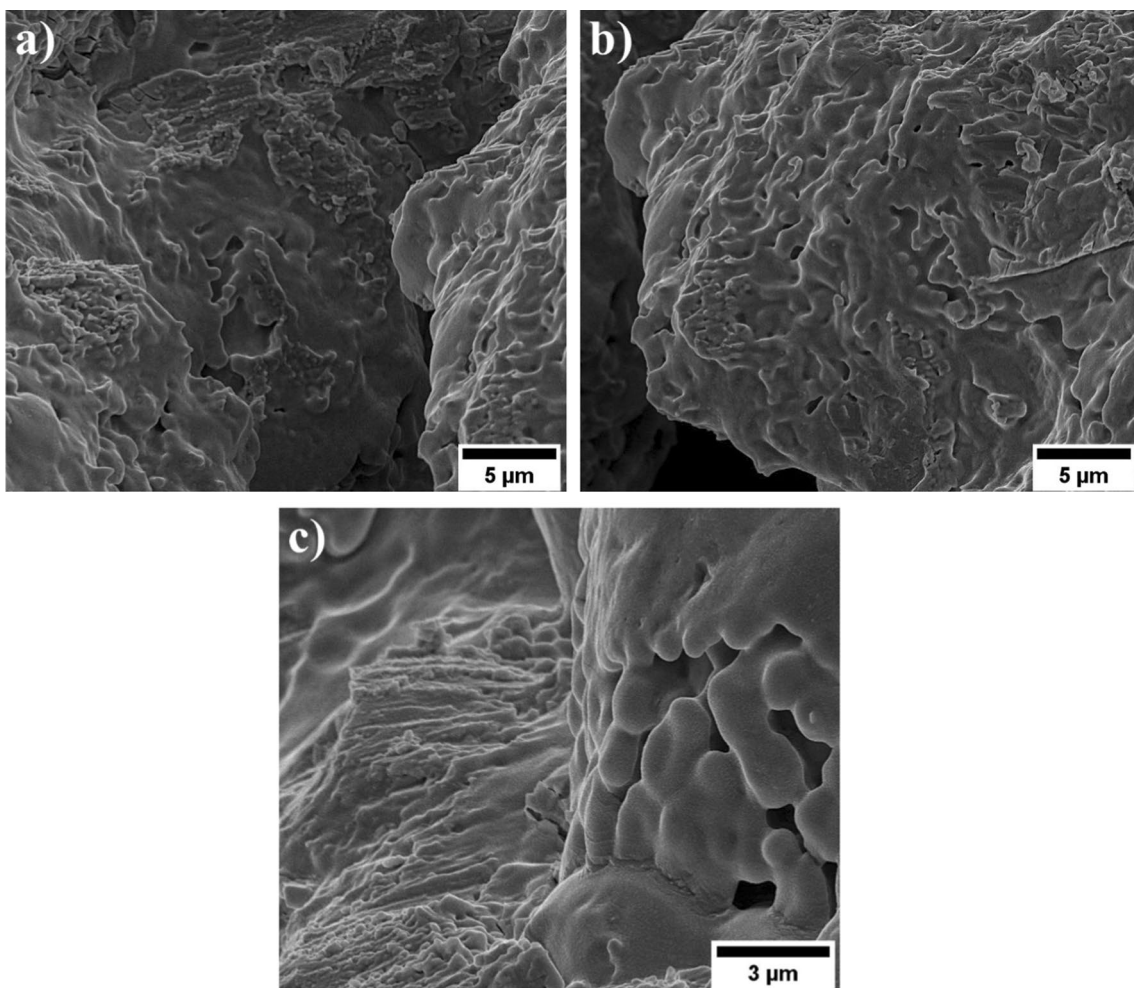
Fig. 26 Liquation crack in the HAZ: **a** Crack cavity, **b** Smooth surface, **c** Numerous fine cavities, SEM-SE

the opposite edge of the crack and form "bridges" (Fig. 26). This excludes the possibility of quasi-hot cracks, as a result of a mechanism other than constitutional liquation. On the smooth surface of the liquation crack, numerous protrusions, concavities, and crevices are observed related to microstructural heterogeneity of deeper eutectic areas. This proves that a relatively low amount of liquid formed during welding. The local change in material volume accompanying welding resulted from thermal expansion and constitutional liquation (solid state→liquid state). In the HAZ at subsolidus temperatures, the solid phase was affected by tensile stresses, which led to an increase in the distance between opposing grains and, in turn, to gap widening. During cooling, the solid phase heterogeneously nucleated on the partially melted grain surface. The accompanying reduction in volume meant that in the final stage of solidification, the eutectic phase grew on the opposite grains but did not come into contact. The resulted in smooth fracture surfaces. With insufficient amounts of liquid present along the grain boundaries, the microcracks remained unhealed.

The thickness of the liquid film along the grain boundaries is a significant feature that can control crack formation during welding. It can improve weldability by influencing the re-solidification temperature range, minimising the amount of stress necessary to cause cracking at a given temperature, while additionally inducing stress relaxation through liquid penetration. Miller and Chadwick [41] suggested that the tensile stresses needed to overcome surface tension (γ_{SL}) on a grain boundary containing a liquid film of a thickness "h" can be described as $\sigma = 2\gamma_{SL}/h$. Increasing the thickness of the liquid film can decrease stress leading to decohesion at the solid/liquid interface. However, the alloy's susceptibility to liquation cracking does not increase proportionally with the liquid film's thickness, as indicated by the relationship above. The limiting thickness is when liquid healing starts, which prevents the propagation of the initiated microcracks. The concept of healing means that in the initial stage of solidification, the interdendritic liquid film may fill the microcracks between the crystallites, thus overcoming harmful effects. When the alloy contains more than a critical amount of liquid volume during solidification, the inflow of the liquid would heal any microcrack created by the contraction of the primary grains. Liquid healing happens when a sufficient amount of intergranular liquid is present to backfill and heal incipient cracks as they develop. The amount of liquid necessary for effective healing may vary from alloy to alloy.

4 Conclusions

This work focussed on analysing the contribution of microstructural constituents in the Renè 108 superalloy on HAZ liquation cracking. The main conclusions are the following:

(1) The material in pre-weld state was characterised by a dendritic structure with microstructural constituent segregation. The dendritic regions mainly consisted of γ' precipitates and M_5B_3 borides at γ/γ' interfaces, while interdendritic spaces additionally contained eutectic $\gamma–\gamma'$ islands, as well as MC and $M_{23}C_6$ carbides.

(2) Based on the ThermoCalc simulation it was observed that under equilibrium condition the γ' solvus temperature is 1281 °C. According to the DSC, the incipient melting in the Renè 108 occurred at 1294 °C.

(3) At 975 °C, the mean UTS was 1107 MPa, at which the maximum area reduction was found to be 6.6%. The high-temperature brittleness range coincides with all test temperatures of 950-NST. The DDR, RDR, and R_f values were 32.1%, 36.2%, and 0.05, respectively. These values testify to the superalloy's low resistance to hot cracking.

(4) The autogenous bead-on-plate process led to liquation crack formation in the HAZ.

(5) A thin layer was observed along the edges of the cracks, indicating that a liquid phase was locally present at elevated temperatures. Rapid heating above the γ' solvus temperature led to the formation of eutectic liquid due to the reaction of partly dissolved γ' precipitates with the matrix. The location of the cracks suggests that M_5B_3 borides and $M_{23}C_6$ carbides could have participated in constitutional liquation. It was found that the role of MC carbides in increasing susceptibility to liquation cracking is not significant.

(6) The $\gamma–\gamma'$ eutectic phase nucleated epitaxially during cooling, on partially melted grains. Liquation crack fractures were characterised by a free surface. Its numerous convexities and concavities indicate to a relatively small amount of liquid being formed by constitutional liquation along the grain boundaries.

Data availability The data that support the findings of this study are available from the corresponding author upon reasonable request.

Declarations

Conflict of interest The authors declare that they have no known competing financial interests or personal relationships that could have appeared to influence the work reported in this paper.

References

1. Gurrappa I, Yashwanth IVS, Gogia AK. The selection of materials for marine gas turbine engines. In: Volkov K, editor. Efficiency, performance and robustness of gas turbines. London: Intech open; 2012. p. 51–70.
2. Sims C. Superalloys II: high-temperature materials for aerospace and industrial power. New York: Wiley; 2014. p. 1987.
3. Reed R, Rae C. Physical metallurgy of the nickel-based superalloy. In: Laughlin D, Hono K, editors. Physical metallurgy. Elsevier; 2014. p. 2215–90.
4. Matysiak H, Zagórska M, Andersson J, Balkowiec A, Cygan R, Rasiński M, Pisarek M, Andrzejczuk M, Kubiak K, Kurzydłowski K. Microstructure of Haynes ®282® superalloy after vacuum induction melting and investment casting of thin-walled components. Mater. 2013;6:5016–37. https://doi.org/10.3390/ma6115016.
5. Rakoczy Ł, Grudzień M, Tuz L, Pańcikiewicz K, Zielińska-Lipiec A. Microstructure and properties of a repair weld in a nickel based superalloy gas turbine component. Adv Mater Sci. 2017;17:55–63. https://doi.org/10.1515/adms-2017-0011.
6. Ojo O, Richards N, Chaturvedi M. Contribution of constitutional liquation of gamma prime precipitate to weld HAZ cracking of cast Inconel 738 superalloy. Scri Mater. 2004;50:641–6. https://doi.org/10.1016/j.scriptamat.2003.11.025.
7. Rakoczy Ł, Grudzień M, Zielińska-Lipiec A. Contribution of microstructural constituents on hot cracking of MAR-M247 nickel based supealloy. Arch Met Mat. 2018;63(1):181–9. https://doi.org/10.24425/118926.
8. Singh S, Andersson J. Hot cracking in cast alloy 718. Sci Technol Weld Join. 2018;23:568–74. https://doi.org/10.1080/13621718.2018.1429238.
9. Taheri M, Razavi M, Kashani-Bozorg SF, Torkmany MJ. Relationship between solidification and liquation cracks in the joining of GTD-111 nickel-based superalloy by Nd:YAG pulsed-laser welding. J Mater Res Technol. 2021;15:5635–49. https://doi.org/10.1016/j.jmrt.2021.11.007.
10. Li Q, Xie J, Yu J, Shu D, Hou G, Sun X, Zhou Y. Solidification behavior and segregation characteristics of high W-content cast Ni-based superalloy K416B. J All Comp. 2021;854:156027. https://doi.org/10.1016/j.jallcom.2020.156027.
11. Lippold J, Kiser S, DuPont J. Welding metallurgy and weldability of nickel-base alloys. New Jersey: Wiley; 2009.
12. Radhakrishnan B. Interface controlled precipitate dissolution and constitutional liquation. Inter Sci. 1993;1:175–82. https://doi.org/10.1007/BF00203607.
13. Grosdidier T, Hazotte A, Simon A. Precipitation and dissolution process in γ/γ' single crystal nickel-based superalloy. Mat Sci Eng A. 1998;256:183–96. https://doi.org/10.1016/S0921-5093(98)00795-3.
14. Hewitt P, Butler E. Mechanisms and kinetics of θ' dissolution in Al-3% Cu. Acta Metall. 1986;34:1163–72. https://doi.org/10.1016/0001-6160(86)90002-7.
15. Standard ISO/TR 17641-3 (2005) Destructive tests on welds in metallic materials — hot cracking tests for weldments — arc welding processes — part 3: externally loaded tests
16. Rakoczy Ł, Milkovič O, Rutkowski B, Cygan R, Grudzień-Rakoczy M, Kromka F, Zielińska-Lipiec A. Characterization of γ' precipitates in cast Ni-based superalloy and their behaviour at high-homologous temperatures studied by TEM and in situ XRD. Mater. 2020;13:2397. https://doi.org/10.3390/ma13102397.
17. Rakoczy Ł, Grudzień-Rakoczy M, Hanning F, Cempura G, Cygan R, Andersson J, Zielińska-Lipiec A. Investigation of the γ' precipitates dissolution in a Ni-based superalloy during stress-free short-term annealing at high homologous temperatures. Metall Mater Trans A. 2021;52:4767–84. https://doi.org/10.1007/s11661-021-06420-4.
18. Goldschmidt H. Effect of boron additions to austenitic stainless steels. J Iron Steel Inst. 1971;209:900–9.
19. Perevislov S, Vysotin A, Shcherbakova O. Studying the properties of carbides in the system ZrC–HfC, TaC–ZrC and TaC–HfC. IOP Conf Ser: Mater Sci Eng. 2020;848:012069. https://doi.org/10.1088/1757-899X/848/1/012069.
20. Singh S, Hanning F, Andersson J. Influence of homogenisation treatments on the hot ductility of cast ATI® 718Plus®: effect of niobium and minor elements on liquation characteristics. Mat Sci Eng A. 2021;799:140151. https://doi.org/10.1016/j.msea.2020.140151.
21. Adamiec J, Konieczna N. Assessment of the hot cracking susceptibility of the Inconel 617 nickel-based alloy. Arch Metall Mat. 2021;66:241–8. https://doi.org/10.24425/amm.2021.134781.
22. Ojo O, Richards N, Chaturvedi M. Contribution of constitutional liquation of gamma prime precipitate to weld HAZ cracking of cast Inconel 738 superalloy. Scr Mater. 2004;50(5):641–6. https://doi.org/10.1016/j.scriptamat.2003.11.025.
23. Rosenthal R, West D. Discontinuous γ'-precipitation in directionally solidified IN 738 LC alloy. Mat Sci Tech. 1986;2:169–74. https://doi.org/10.1179/mst.1986.2.2.169.
24. Sponseller D. Differential thermal analysis of nickel-base superalloys. In: Kissinger R, editor. Superalloys, 1996. Pennsylvania: TMS (The Minerals, Metals & Materials Society); 1996. p. 259–70.
25. Ojo OA, Richards NL, Chaturvedi MC. Contribution of constitutional liquation of gamma prime precipitate to weld HAZ cracking of cast Inconel 738 superalloy. Scr Mat. 2004;50:641–6. https://doi.org/10.1016/j.scriptamat.2003.11.025.
26. Ojo O, Richards N, Chaturvedi M. Liquid film migration of constitutionally liquated γ' in weld heat affected zone (HAZ) of Inconel 738LC superalloy. Scr Mater. 2004;51:141–6. https://doi.org/10.1016/j.scriptamat.2004.03.040.
27. Kotval PS, Venables JD, Calder RW. The role of hafnium in modyifying the microstructure of cast nickel-base superalloys. Metall Mat Trans B. 1972;3:457–62. https://doi.org/10.1007/BF02642049.
28. Jingwei C, Salvati E, Uzun F, Papadaki C, Wang Z, Everaerts J, Korsunsky AM. An experimental and numerical analysis of residual stresses in a TIG weldment of a single crystal nickel-base superalloy. J Manuf Proc. 2020;53:190–200. https://doi.org/10.1016/j.jmapro.2020.02.007.

29. Baeslack WA III, West SL, Kelly TJ. Weld cracking in Ta-modified cast Inconel 718. Scri Metall. 1988;22:729–34. https://doi.org/10.1016/S0036-9748(88)80191-1.

30. Aritonang S, Ezha Kurniasari WS, Juhana R, Herawan T. Analyzing tantalum carbide (TaC) and hafnium carbide (HfC) for spacecraft material. In: Zahid M, Sani A, Mohamad Yasin M, Ismail Z, Lah N, Turan F, editors. Recent trends in manufacturing and materials towards industry 4.0. Lecture notes in mechanical engineering. Singapore: Springer; 2021.

31. Bai G, Li J, Hu R, Zhang T, Kou H, Fu H. Effect of thermal exposure on the stability of carbides in Ni-Cr-W based superalloy. Mat Sci Eng A. 2011;528:2339–44. https://doi.org/10.1016/j.msea.2010.11.088.

32. Li S, Li K, Hu M, Wu Y, Cai Z, Pan J. The mechanism for HAZ liquation of nickel-based alloy 617B during gas tungsten arc welding. Metals. 2010;10:94. https://doi.org/10.3390/met10010094.

33. Després A, Antonov S, Mayer C, Tassin C, Veron M, Blandin J, Kontis P, Martin G. On the role of boron, carbon and zirconium on hot cracking and creep resistance of an additively manufactured polycrystalline superalloy. Mater. 2021;19:101193. https://doi.org/10.1016/j.mtla.2021.101193.

34. Grodzki J, Hartmann N, Rettig R, Affeldt E, Singer RF. Effect of B, Zr, and C on hot tearing of a directionally solidified nickel-based superalloy. Metall Mater Trans A. 2016;47:2914–26. https://doi.org/10.1007/s11661-016-3416-8.

35. Osoba L. A study on laser weldability improvement of newly developed Haynes 282 superalloy. PhD thesis, University of Manitoba, 2012

36. Straumal A, Yardley V, Straumal B, Rodin A. Influence of the grain boundary character on the temperature of transition to complete wetting in the Cu-In system. J Mater Sci. 2015;50:4762–71. https://doi.org/10.1007/s10853-015-9025-x.

37. Straumal B, Kilmametov A, Mazilkin A, Gornakova A, Fabrichnaya O, Kriegel M, Rafaja D, Bulatov M, Nekrasov A, Baretzky B. Formation of the ω phase in the titanium-iron system under shear deformation. JETP Lett. 2020;111(10):568–74.

38. Straumal B, Korneva A, Kuzmin A, Lopez G, Rabkin E, Straumal A, Gerstein G, Gornakova A. The grain boundary wetting phenomena in the Ti-containing high-entropy alloys: a review. Metals. 2021;11(11):1881. https://doi.org/10.3390/met11111881.

39. Radhakrishnan B, Thompson RG. Liquid film migration (LFM) in the weld heat affected zone (HAZ) of a Ni-base superalloy. Scr Metall Mater. 1990;24:537. https://doi.org/10.1016/0956-716X(90)90197-O.

40. Ojo OA, Richards NL, Chaturvedi MC. Microstructural characterization of Incoloy 903 weldments. Metall Mater Trans. 1993;24:1169–79. https://doi.org/10.1007/BF02657248.

41. Miller WA, Chadwick GA. On magnitude of solid/liquid interfacial energy of pure metals and its relation to grain boundary melting. Acta Met. 1967;15:607–14. https://doi.org/10.1016/0001-6160(67)90104-6.